CHAPTER 1

Hydrogen Reactions on Nanostructured Surfaces

HOLGER WOLFSCHMIDT and ODYSSEAS PASCHOS

Department of Physics, Technische Universität München, Garching, Germany

ULRICH STIMMING

Department of Physics, Technische Universität München and ZAE Bayern Division 1, Garching, Germany

Hydrogen catalysis is an important scientific field since hydrogen reactions (e.g., hydrogen evolution and hydrogen oxidation) play a key role in electrochemical devices such as fuel cells and electrolyzers. The latter devices have the potential to provide clean and sustainable energy with high efficiencies. This chapter reviews hydrogen catalysis in detail. Details on hydrogen reaction studies from theoretical and experimental perspectives are presented. The former usually complement the results from experimental studies and are used to strengthen them. Various systems that have been explored throughout the years are reviewed. These include model surfaces as well as applied systems. Model catalyst systems comprise Pt and Pd nanoislands deposited on planar surfaces of inert supports, high-quality single-crystal materials, or single nanoparticles created with scanning tunneling microscopy tips. Applied systems consist of metallic nanoparticles deposited on high-surface-area carbon supports. Theory versus experiment, and model versus applied systems are reviewed in detail, and useful insights for hydrogen reactions in these systems are demonstrated

1.1 INTRODUCTION

Whereas the nineteenth century was the stage of the steam engine and the twentieth century was the stage of the internal-combustion engine, it is likely that the twenty-first century will be the stage of the fuel cell. Fuel cells have captured the interest of people

Fuel Cell Science: Theory, Fundamentals, and Biocatalysis,
Edited by Andrzej Wieckowski and Jens K. Nørskov

around the world as one of the next great energy alternative. They are now on the verge of being introduced commercially, revolutionizing the present method of power production. Fuel cells can use hydrogen as fuel and oxygen or air as oxidant, offering the prospect of supplying the world with clean, sustainable electrical power, heat, and water.

This chapter focuses on hydrogen reactions such as the hydrogen oxidation reaction (HOR) and the hydrogen evolution reaction (HER). These reactions are of utmost importance in developing and improving fuel cell devices. The discussion here is directed principally toward hydrogen electrocatalysis from an experimental as well as theoretical perspective. Starting with an overview on the fundamentals of hydrogen reactions in Section 1.2, studies on single crystals as well-defined and high-quality surfaces are reviewed. An introduction to theoretical work calculating important fundamentals for hydrogen catalysis regarding material properties is then discussed. As predicted by theory, the behavior of nanostructured and bimetallic surfaces differs from that of bulk material. Similar findings supporting the theoretical predictions are shown for large nanostructured surfaces as well as single particles. The section concludes with a short overview of carbon-based catalysts.

The fundamentals of hydrogen reactions are reviewed in Section 1.2. Starting from the general reversible hydrogen reaction, the different reaction pathways suggested by Volmer, Heyrowsky, and Tafel are introduced. Because of the importance of the hydrogen adsorption mechanism and the important findings with new experimental techniques, a short overview of results obtained since the late 1990s is given. An introduction to the correlation between catalytic behavior and the catalyst material significance of this correlation, completes this section using experimental and theoretical calculations, with a conclusion regarding the long-range.

Single crystals and well-defined surfaces play a very important role in surface science. Many scientific contributions are available that study these well-defined surfaces. Section 1.3 introduces the electrochemical behavior toward hydrogen reactions on Pt, Au, and Pd surfaces. The quality of single crystals rapidly increased in the 1990s, resulting in new and different insights. Because of the importance of Pt as a catalyst, the main part of this section focuses on this element. The dependence of the crystallographic orientation toward adsorption as well as electrocatalytic activity is discussed. An introduction to Pd as a catalyst material with the property to absorb hydrogen and Au as an inert support material is the last topic in that section.

Besides experimental work, numerous theoretical calculations for hydrogen catalysis have been performed. Computational methods such as density functional theory (DFT) and Monte Carlo simulations are powerful tools in surface science and catalysis. Theoretical as well as experimental work has been combined in several scientific publications and complement each other well. The first principles of theoretical techniques and theoretical results are shown in Section 1.4. As a main topic, the adsorption behavior of hydrogen is considered and the *d*-band model is introduced. Calculations regarding the hydrogen oxidation reaction and the influence of different reactions pathways are also shown. Theoretical calculations of metals on thin films and supported on various foreign metals are reviewed and are correlated with experimental findings.

The chemical behavior of metal nanoparticles often differs from that of bulk metal. Different effects such as particle size, interparticle distance, and support effects have to be considered in this nanometer-scale regime. Since Pd and Pt are important materials in catalysis, much work was done in the last few decades describing the abovementioned effects. In particular, multilayers, monolayers, and submonolayers of Pd and Pt onto foreign metal supports have shown unexpected behavior. Pd on Au(111) regarding several electrochemical properties introduces this section. Different types of adsorption, absorption, and desorption behavior as well as electrocatalytic activity toward hydrogen reactions are shown and discussed. The deposition of Pd on other supports and the influence of hydrogen reactions hindered by adsorbing foreign adsorbates as well as investigations of Pt overlayers on Au(111) are also discussed. A summary and detailed discussion in Section 1.5 also includes theoretical aspects.

As mentioned above, planar surfaces are thoroughly investigated and serve as widely accepted reference systems with high-quality, reproducible results. For local investigation of small structures, new approaches and setups have to be designed and applied. For this purpose, the electrochemical scanning tunneling microscope (EC-STM) has been modified by several groups in order to create small nanoparticles and nanoparticle arrays and also to investigate corrosion, deposition, dissolution, and reactivity. Due to the tunneling effect, high resolution is achievable and thus leads to a precise technique with atomic resolution. The STM tip can be used in different ways in the electrochemical environment to create and investigate local reactivity of nanostructures. Experimental and theoretical results are compared and are shown to complement each other. Specifically, the activity of a single Pd particle is shown. A discussion of the experimental results of the stability of Pd particles deposited on Au (111) and their reactivity toward HER follows. A summary completes Section 1.6 with a comparison between results obtained at extended Pd nanostructured Au(111) surfaces and single Pd particles.

Section 1.7 presents an overview of studies performed on carbon-based systems. Since carbon has high electrical conductivity, is relatively inexpensive to use, and is highly available, it has been the favored support material for many years. Of the many scientific contributions, only a few can be presented here regarding the mechanism of HER and HOR using metallic nanoparticles with carbon-based supports. The reactivity of these catalysts for hydrogen reactions and CO oxidation is also of major interest. These catalyst systems include glassy carbon, carbon nanofibers, Vulcan, and carbon black for support for metallic nanoparticles, and the more highly oriented and defined pyrolytic graphite (HOPG) are also presented and discussed.

1.2 FUNDAMENTALS OF HYDROGEN REACTIONS

1.2.1 Hydrogen Catalysis

Over the years a number of studies have been performed in order to investigate the characteristics of hydrogen-related reactions. The general reversible reaction is as follows:

$$H^+ + e^- \leftrightarrow \tfrac{1}{2}H_2 \tag{1.1}$$

Its standard potential is set to 0 V. In the case of proton discharge to form molecular hydrogen the reaction is called a *hydrogen evolution reaction* (HER), while the reverse pathway describes the *hydrogen oxidation reaction* (HOR). However, for the reaction to proceed at sufficient rate, it needs to be catalyzed on an electrode surface. Possible catalyst candidates include various metals such as Pt, Pd, and Ru, as well as enzymes with active centers. Much research focused on finding parameters that influence the activity of materials toward hydrogen electrocatalysis. Even though much progress has been made on this matter, it is still not clearly known how various properties influence the catalytic activity. More details will be given later in this section.

Today it is generally accepted that hydrogen evolution on Pt occurs via two different pathways consisting of every two reaction steps:

Discharge reaction of a proton to form an adsorbed hydrogen atom, known as the *Volmer reaction* [1]:

$$Pt + H^+ + e^- \rightarrow H{-}Pt \tag{1.2}$$

Combination of two adsorbed hydrogen atoms to form molecular hydrogen, known as the *Tafel reaction* [2]:

$$2(H{-}Pt) \rightarrow H_2 + 2Pt \tag{1.3}$$

Combination of an adsorbed hydrogen atom with a proton and an electron to form molecular hydrogen, known as the *Heyrovsky reaction* [3]:

$$H{-}Pt + H^+ + e^- \rightarrow H_2 + Pt \tag{1.4}$$

Two different pathways can occur; the first one is described as a combination of reactions (1.2) and (1.3), known as the *Volmer–Tafel mechanism*. With this mechanism, protons from the solution are discharged on the catalyst surface, forming adsorbed hydrogen atoms. Then, two adjacent adsorbed hydrogen atoms combine to form molecular hydrogen. The second mechanism, known as the *Volmer–Heyrovsky mechanism*, can be described by combining reactions (1.2) and (1.4). A proton from electrolyte solution is discharged on the catalyst surface to form an adsorbed hydrogen atom. This step is followed by combination with another proton and electron to form molecular hydrogen.

Hydrogen oxidation reaction on Pt can be described in a similar way using the reaction pathways in reverse order:

Dissociation of molecular hydrogen into one adsorbed hydrogen atom and immediate discharge of the other atom into proton and electron, similar to the Heyrovsky reaction:

$$H_2 + Pt \rightarrow H{-}Pt + H^+ + e^- \tag{1.5}$$

Adsorption of molecular hydrogen on the catalyst surface in the form of two hydrogen atoms, similar to the Tafel reaction:

$$H_2 + 2Pt \rightarrow 2(H{-}Pt) \tag{1.6}$$

Discharge of an adsorbed hydrogen atom to proton and electron, similar to the Volmer reaction:

$$H{-}Pt \rightarrow Pt + H^+ + e^- \tag{1.7}$$

Similar to hydrogen evolution, the hydrogen oxidation reaction can follow two different pathways. The first mechanism is a combination of reactions (1.5) and (1.7). A hydrogen molecule is positively charged ($H_2 \rightarrow H_2^+$), and immediately one of its atoms is discharged into proton and electron, while the other is adsorbed on the surface of the catalyst. Then the adsorbed hydrogen atom is discharged into proton and electron. The second one is a combination of reactions (1.6) and (1.7). With this mechanism molecular hydrogen is adsorbed on the catalyst surface in the form of two hydrogen atoms, followed by discharge of the atoms into proton and electron.

1.2.2 Hydrogen Adsorption Mechanism and Experimental Setups

As was shown above, in both hydrogen reactions (oxidation and evolution) the step of forming a hydrogen adsorbate on the catalyst surface exists in both pathways. Research was performed in order to study the mechanism of hydrogen adsorption on Pt single crystals. Pt is one of the most widely studied catalysts because of its ability to catalyze hydrogen reactions with small overpotentials. Initial studies focused on determining the heat of adsorption of hydrogen on Pt(111) single crystals. An interesting review was published by Markovic and Ross [4], who showed the values for the heat of hydrogen adsorption reported in early years to be inconsistent. Christmann and Ertl [5] reported in 1976 that the value for Pt(111) is approximately equal to 50–60 kJ/mol. However, McGabe and Schmidt [6] in 1977 and Salmeron et al. [7] in 1979 reported higher values, between 70 and 90 kJ/mol. Later, it was found that these corresponded to adsorption of hydrogen on defect sites. Until relatively recently it was accepted that hydrogen tends to adsorb on highly coordinated sites, which for the case of Pt(111) would be the threefold hollow sites. These would lead, though, to a very high coverage of two hydrogen atoms per Pt; therefore, in order to ensure agreement with experimental values, it was accepted that hydrogen occupies the threefold next-nearest-neighbor sites (for details, see Section 1.3). Olsen et al. [8], performing DFT calculations, showed that hydrogen tends to occupy the top sites. Nevertheless, in all cases the values reported were close to each other.

Depending on the overpotential, the adsorbed hydrogen atom on the catalyst surface is referred to as *under-* or *overpotential deposited hydrogen* (H_{upd} or H_{opd}). H_{upd} refers to hydrogen atoms adsorbed at potentials positive of the reversible hydrogen electrode (RHE) potential, while H_{opd} occurs at potentials negative of the RHE potential. The state of H_{upd} and H_{opd} depends also on the pH of the electrolyte and

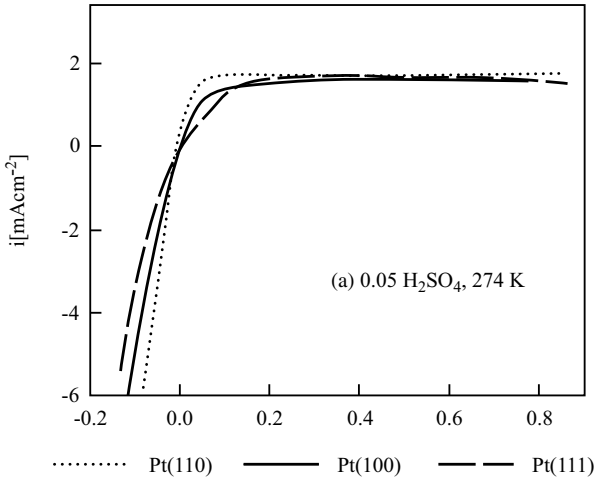

FIGURE 1.1 Polarization curves for HER and HOR on Pt(*hkl*) in 0.1 M $HClO_4$ at sweep rate 20 mV/s [4].

is generated from either protons or water molecules [4] and can be described by the following reactions:

$$Pt + H_3O^+ + e^- \rightarrow Pt{-}H_{upd} + H_2O \quad (pH \leq 7) \tag{1.8}$$

$$Pt + H_2O + e^- Pt{-}H_{upd} + OH^- \quad (pH \geq 7) \tag{1.9}$$

There are several possible reasons why reported experimental values sometimes do not agree. The first would be the quality of the single crystal. Crystals having defect sites or impurities adsorbed on their surfaces act differently toward electrochemical reactions. Also, it has been shown that different single crystal faces of Pt have different electrocatalytic rates. Markovic and Ross [4] showed that the activity increases in the order of (111) < (100) < (110) (Fig. 1.1).

Barber et al. [11] showed a slightly different result (Fig. 1.2), where the activity for HER/HOR increases in the order of (100) < (111) < (551) < (110).

However, despite these small differences, it is clearly shown that the activity is strongly affected by the orientation of the Pt single crystal.

The experimental technique also plays a determining role on the results obtained mainly with the appearance of a limiting current density above certain overpotentials for the hydrogen reactions. Especially for the case of HOR on Pt, the exchange current density is high in acidic solutions, but simultaneously, because of the low solubility of hydrogen, the limiting diffusion current is low. Quaino et al. [12] showed that by using Levich–Koutecky analysis the $j(\eta)$ dependence for HOR cannot always be obtained accurately and may be underestimated. Bagotzky and Osetrova [13] were the first to propose an alternative experimental setup that had the potential to solve many issues related to the investigation of HOR. Their setup consisted of Pt microelectrodes

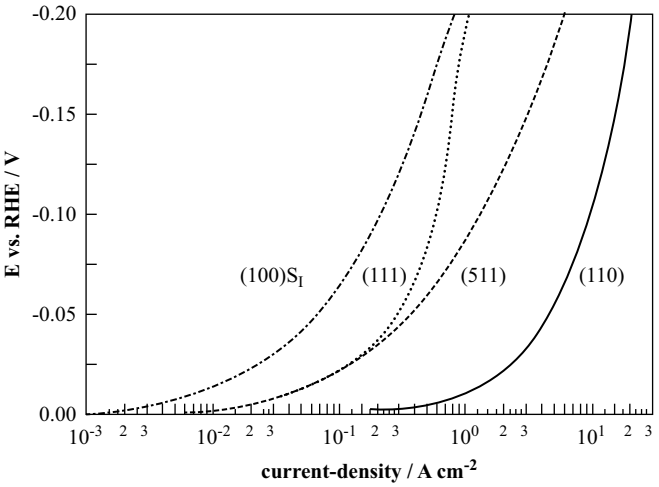

FIGURE 1.2 Derived Tafel plots, less the diffusion effect, for the Pt (100)S_I, (511), (111), and (110) faces as marked on the plot [11].

('A' and 'B') embedded in fused-glass tubes with two different polished surfaces. Because of the small thickness of the electrode, there was an enhanced mass transport of hydrogen. Therefore, values for limiting diffusion current that were one order of magnitude higher than those obtained from RDE setups could be reached. However, the results obtained were affected by the roughness of the microelectrode surface, which can be clearly seen in Figure 1.3.

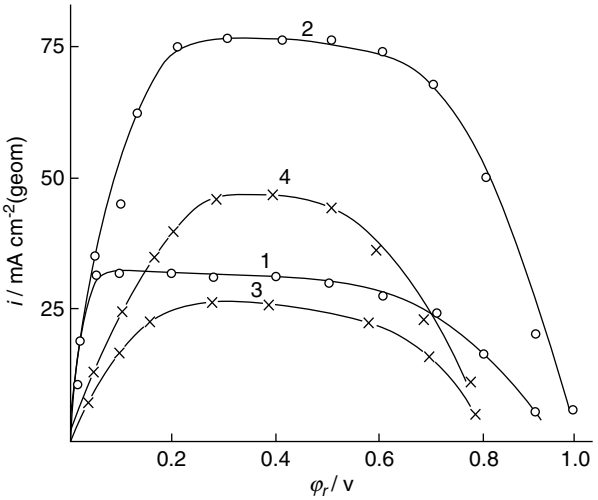

FIGURE 1.3 Dependence of hydrogen ionization current on potential on microelectrodes with different roughness values *A* and *B* in 0.5 M H_2SO_4: (1) *A*, (2) *B* and in 1 M KOH: (3) *A*, (4) *B* [13].

Two electrodes with different roughness values, differentiated by the degree of polishing, were used to study hydrogen oxidation in both acidic and alkaline solutions, and as can be seen, the results are different for the two electrodes. Quaino et al. [14] used a similar setup to study hydrogen oxidation. They were able to demonstrate that at low overpotentials the Tafel–Volmer route dominates the kinetics of HOR. At high overpotentials the Tafel–Volmer effect diminishes while the Volmer–Heyrovsky mechanism becomes dominant.

Also, traces of impurities that can be present in unpurified solutions can compete with the reactions under certain conditions, especially at low current densities [15], resulting in misleading interpretation of the results.

1.2.3 Correlation between Activity toward Hydrogen Reactions and Physicochemical Properties of Catalyst Material

In the early years research was focused on finding a relationship between the activity toward hydrogen evolution and oxidation and a property of the catalyst. Conway and Bockris [16] reported a correlation between the exchange current density j_0 and the electronic workfunction *f*. *Workfunction* is defined as the energy with which electrons near the Fermi level are bound to the material. According to their study [16], the relationship between j_0 and *f* arises from the dependence of heat of adsorption on *f*. Additionally, they showed that the bond strength between adsorbed hydrogen and metal calculated from Pauling's equation was smaller than the one obtained from experiments. They also, as can been seen in Figure 1.4, using values from the literature, demonstrated that for various metals (e.g., Ta, Mo, W, Cu, Ni, Fe, Rh, Pd, Pt) the logarithm of j_0 increases as the heat of adsorption of H decreases, while an opposite trend is observed for Hg, Cd, Pb, and Tl.

For HER, it was also shown (Fig. 1.5) that the logarithm of j_0 increases as the *d* character of the material increases.

The latter was explained by the fact that as the *d* character increases, more electrons have paired spins and hence require more energy to extract, them causing ΔH of adsorbed hydrogen atoms to decrease.

Parsons [17] studied the relationship between exchange current density and the ability of the electrode to adsorb atomic hydrogen in terms of the standard free energy ΔG_{H}. His theoretical studies showed that log j_0 reaches a maximum when $\Delta G_{\mathrm{H}} \sim 0$. Even though he mentions a disagreement between experimental and theoretical results (a similar disagreement is also mentioned by Trasatti [18] for the heat of adsorption, the observed trend should still be valid. Metals that adsorb hydrogen weakly (ΔG_{H} has positive values), such as Hg, Zn, and Sn, have low exchange current densities. Metals such as Pt that adsorb moderately hydrogen have high values of j_0 and metals that adsorb hydrogen strongly, such as Mo, Ta, and W, also have low j_0 values.

It was shown that there is dependence between the exchange current density for hydrogen reactions and the workfunction of the catalyst material. However, workfunction values were usually used by electrochemists as obtained from physical experiments. These values were usually measured using nonelectrochemical inputs

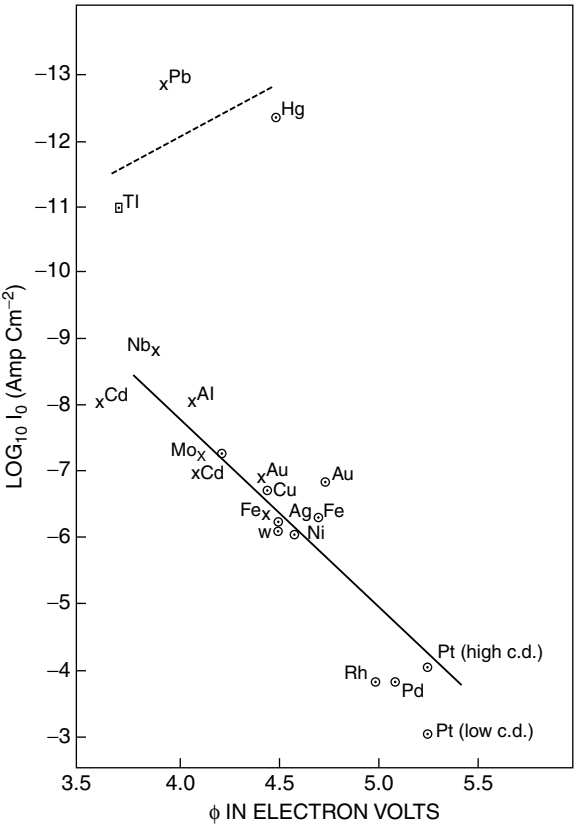

FIGURE 1.4 Linear dependence of $\log_{10}$ of the exchange current (i_0) of HER on the electronic workfunction *f*. Values of $\log_{10} i_0$ are taken from the literature [16].

such as adsorption of gas hydrogen on metals and without taking into consideration the chemical environment surrounding the catalyst. Trasatti [18] published an interesting review on several aspects in order to obtain more accurate data regarding the correlation of hydrogen reactions to physicochemical properties of materials. He argued that the sign of the charge of electrode surface is usually ignored. If the exchange current density j_0 is plotted versus the workfunction (Fig. 1.6), then two fairly parallel lines can be obtained.

One line consists of data from transition metals and *sp* metals with positively charged surfaces, while the other includes data from *sp* metals with negatively charged surfaces. It is also noteworthy that the lines are approximately 0.4 eV apart from each other. Trasatti explained the division of materials in these two groups in terms of orientation of water molecules on the catalyst surface. As is shown in Figure 1.7, if the surface is positively charged, then water will be positioned with an oxygen atom toward the metal, whereas in the case of a negatively charges catalyst surface, an opposite orientation is expected.

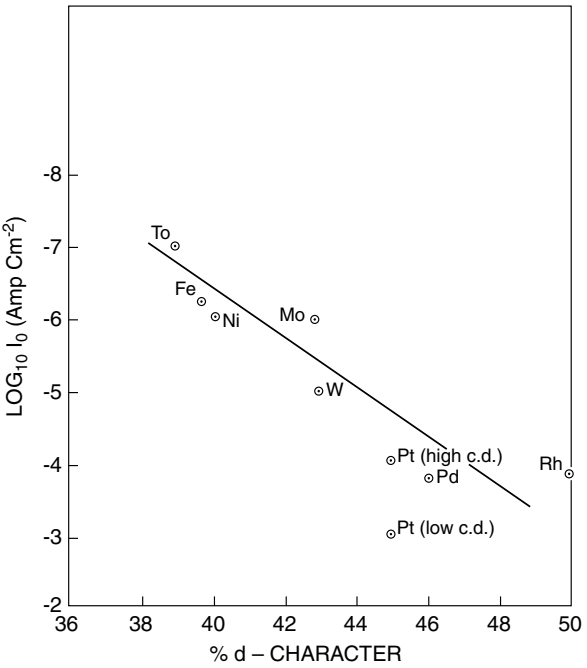

FIGURE 1.5 $\text{Log}_{10}\, i_0$ for HER as a function of percent *d* character of the metal [16].

Although the plot shows a clear difference between transition and *sp* metals, it includes no information regarding the mechanism of reaction. This information can be factored in only if the exchange current density is plotted versus the heat of adsorption of hydrogen on the metal surface. As mentioned previously, the rate and mechanism of HER depends on the bond strength between the metal and the hydrogen atom (M−H). Parsons reported that it should pass through a maximum, and a similar volcano-shaped curve was reported by Krishtalik and Delahay [19], as shown in Figure 1.8.

As shown in Figure 1.8, Pt is on the top of the volcano curve where the Pt−H bond is neither too strong nor too weak. The general trend observed in the volcano curve is that for several metals, as the bonding energy of hydrogen to the metal increases, the activity also increases, reaching a maximum. Then an opposite trend is observed, where log j_0 decreases as the bonding strength of hydrogen to the metal increases.

A similar study was done by Nørskov et al. [20]. Density functional theory (DFT) calculations demonstrated a volcano-type behavior of hydrogen chemisorption energies with respect to exchange current density for hydrogen evolution (Fig. 1.9).

Platinum was again found to be a better catalyst than other metals for HER primarily because hydrogen evolution reaction on Pt is thermoneutral at the equilibrium potential. The findings of this work can be used to predict behavior of other bimetallic systems for HER as well as HOR. The analysis was reported as a new method to obtain H adsorption free energies and understand trends for different systems that are of electrochemical interest.

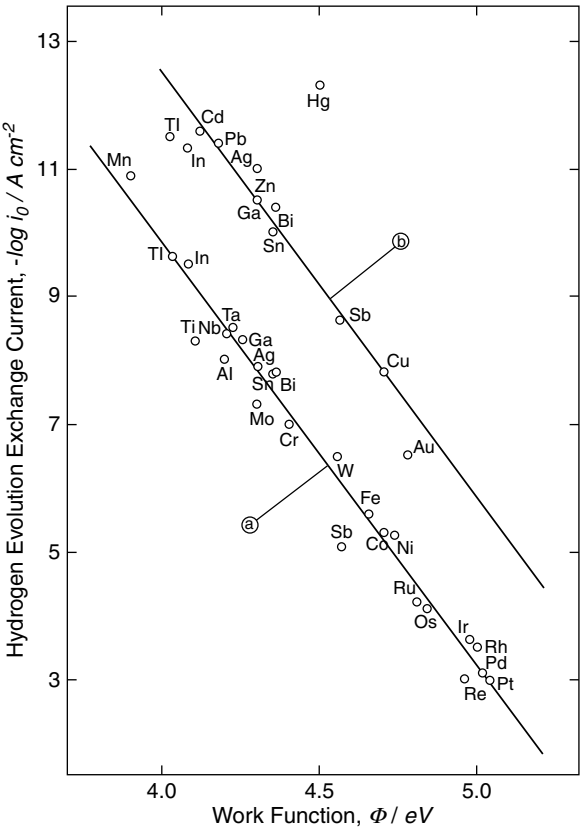

FIGURE 1.6 Exchange currents for HER versus workfunction of metals [18].

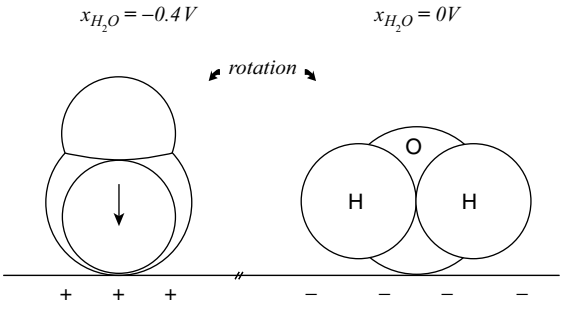

FIGURE 1.7 Drawing of water molecules in position of maximum and minimum orientation suggested as occurring on positively and negatively charged metal surfaces, respectively [18].

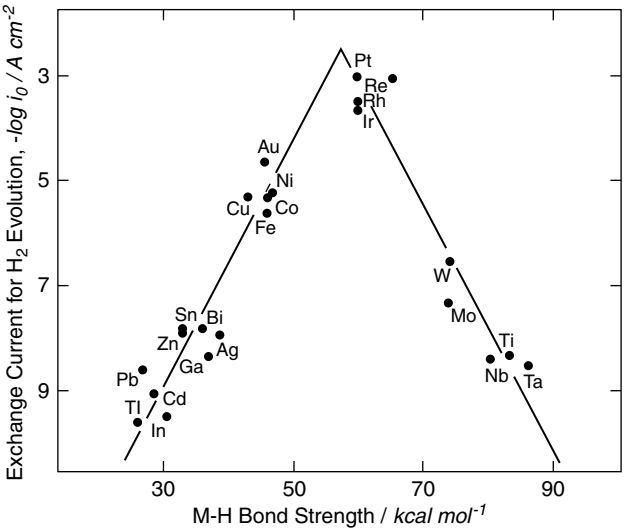

FIGURE 1.8 Exchange currents for HER versus strength of intermediate metal–hydrogen bond formed during electrochemical reaction [18].

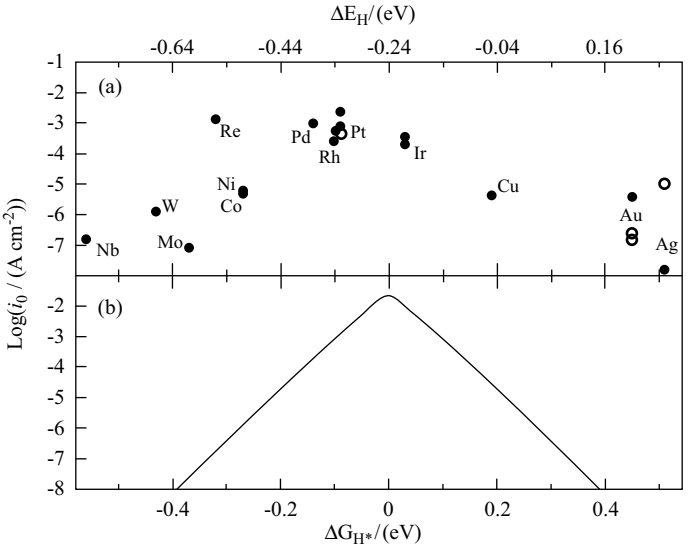

FIGURE 1.9 (a) Experimentally measured exchange current $\log(i_0)$ for HER over different metal surfaces plotted as a function of calculated hydrogen chemisorption energy per atom, ΔE_H (top axis). Open symbols indicate data for single crystals. Results obtained for the simple kinetic model are plotted as a function of the free energy for hydrogen adsorption, $\Delta G_{H^*} = \Delta E_H + 0.24\,\text{eV}$ [20].

1.3 FUNDAMENTAL STUDIES OF HYDROGEN REACTIONS ON EXTENDED SINGLE-CRYSTAL SURFACES

1.3.1 Introduction

Extended well-defined surfaces such as single-crystal surfaces play an important role in surface science by providing accurate and precise systems. Especially in the case of electrochemistry, usage of single crystals has yielded new findings. Hydrogen reactions have been intensively studied have been on polycrystalline as well as single-crystal electrodes. Although the quality of single crystals [21–25] and experimental conditions rapidly increased in the 1990s, fundamental studies started long before [26–29]. Because of the high catalytic activity, Pt and Pd surfaces are of special interest. The main focus of this section is on Pt single crystals and the dependence of crystallographic orientation on electrocatalytic activity. Then Au is also be reviewed, although less work has been performed as compared to Pt. Because of the inertness and low activity of gold and the uncomplicated procedure to prepare Au single crystals, gold is often used as a support for depositing foreign metals, enzymes, and so on. Section 1.3.6 presents a brief introduction to Pd single crystals and Pd overlayers.

1.3.2 Pt(*hkl*) Surfaces

Because of the high degree of catalytic activity of Pt toward several reactions such as hydrogen evolution, hydrogen oxidation, oxygen reduction, and methanol oxidation, Pt is used as a catalyst in various applications. Studies of Pt on polycrystalline and single-crystal surfaces began in the 1970s or so. Annealing as a preparation method for Pt single crystals is widely described in the literature [30, 31]. It was also found that the cooling procedure following the annealing process is important for a well-defined structure. By applying the right annealing and cooling procedures, one can observe specific peaks in the hydrogen region in cyclic voltammograms [32–35], and typical surface structures can be observed via STM [36–38].

Typical voltammograms of Pt(111), Pt(100), and Pt(110) in 0.1 M H_2SO_4 are shown in Figure 1.10. The following discussion concentrates on important findings on Pt(111). Details for Pt(100) and Pt(110) surfaces can be found elsewhere [37–43]. The characteristic current peak at 0.19 V versus SCE in the voltammogram of Pt(111) in 0.1 M H_2SO_4 is caused by a rearrangement in the adsorbed sulfate ion adlayer [44] and can be seen as a parameter for the quality of the single crystal. The ordered (3×7) $R19.1^\circ$ adlayer of these sulfate ions can be observed via STM, which was first demonstrated by Funtikov et al. [45,46]. Comparing the Pt(111) in 0.1 M $HClO_4$ and in 0.1 M H_2SO_4 shows no differences in cyclic voltammograms below 0.1 V versus SCE, indicating a weak influence of anions in this region.

Platinum surfaces were studied regarding electrocatalytic activity on polycrystalline electrodes or poorly defined single crystals [26–29]. Well-defined single-crystal surfaces with unique properties and clean experimental conditions, which are absolutely necessary for electrochemical investigations on Pt surfaces, were established in the 1990s. The hydrogen reactions were intensively investigated on polycrystalline as

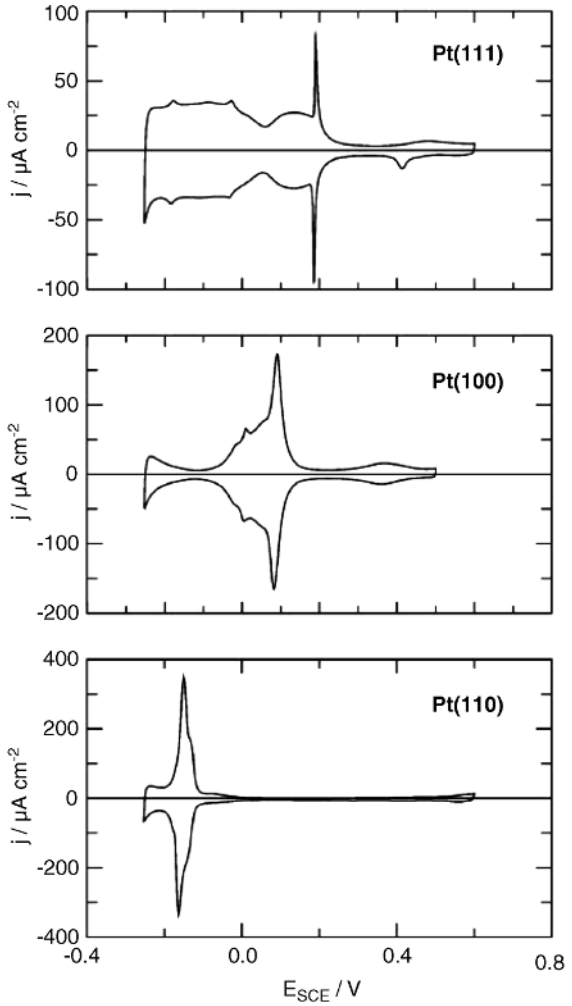

FIGURE 1.10 Cyclic voltammograms for freshly prepared Pt(111), Pt(100), and Pt(110) in 0.1 M H_2SO_4 after cooling in a CO atmosphere and oxidative stripping of the CO adlayer; scan rate 50 mV/s [47].

well as single-crystal surfaces. In early measurments no dependence on crystallographic orientation for electrocatalytic activity was found, which was attributed mainly to poor-quality single crystals and unfavorable experimental conditions. These findings were disproved by Markovic et al. [21,22] and Barber et al. [23,25], who found that the reactivity of different Pt(*hkl*) surfaces toward hydrogen reactions is strongly influenced by surface orientation. It was clearly shown that in alkaline as well as acidic electrolytes, reactivity increases in the order (111) < (100) < (110), as shown in Figure 1.11. In acidic solution the exchange current density of Pt(110) surfaces is 3 times higher than that of Pt(111). The findings are in line with the activation energies

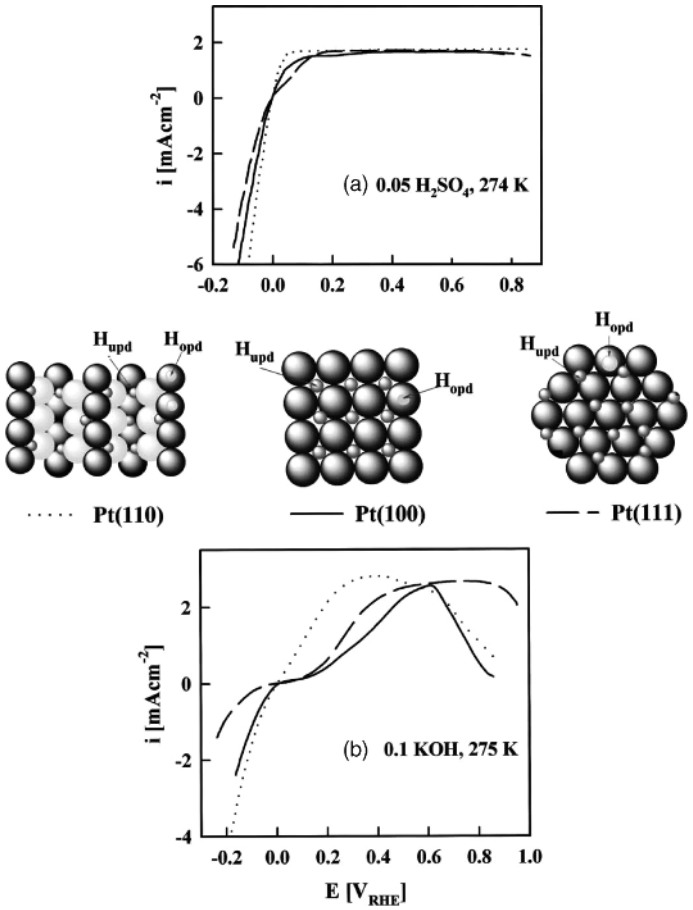

FIGURE 1.11 (a) Polarization curves for HER and HOR on Pt(*hkl*) in 0.05M H_2SO_4 at sweep rate 20 mV/s [2]; (b) polarization curves for HER and the HOR on Pt(*hkl*) in 0.1 M KOH at sweep rate 20 mV/s [1]. Insets show ideal models for the Pt(111)-(1 × 2), Pt(100)-(1 × 1), and Pt(110)-(1 × 1) surfaces; small dots represent the active sites for H_{upd} and H_{opd} [48].

obtained from Arrhenius plots [21] showing the high value of 18 kJ/mol for Pt(111) and the lowest value of 9.5 kJ/mol for the Pt(110) single-crystal surface seen in Figure 1.12.

Arrhenius plots were also used to evaluate the hydrogen evolution in frozen aqueous electrolytes on different polycrystalline metal electrodes [50,51]. Frese et al. [50] investigated HER on polycrystalline Pt electrode in liquid phase and in frozen electrolyte at temperatures ranging between 293 and 176 K. In liquid phase as well as in frozen phase, the Volmer–Tafel mechanism occurs with the Tafel reaction as the rate-determining reaction. An Arrhenius plot (Fig. 1.13) in their paper [50] manifests a linear behavior before and after the melting point of the electrolyte at

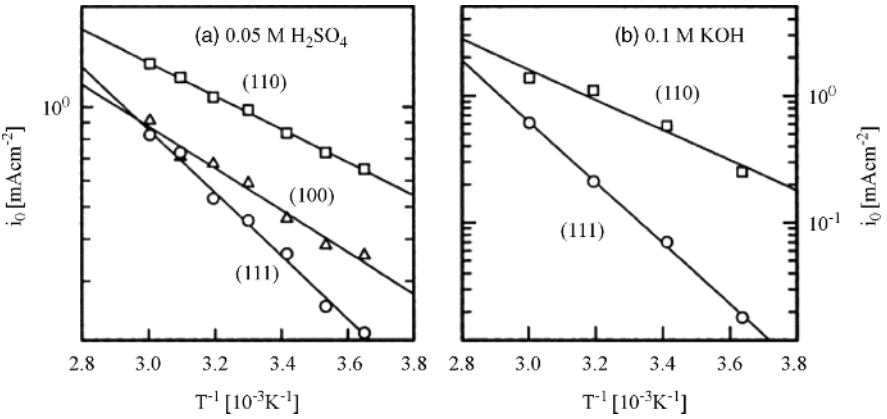

FIGURE 1.12 Arrhenius plots of the exchange current densities (i_0) for HER/HOR on Pt(*hkl*) in (a) acid solution [49] and (b) alkaline solutions [48].

$\sim$227 K. The activation energies are in the range of 15 kJ/mol for the liquid electrolyte and 27 kJ/mol in the frozen electrolyte, clearly seen in the change of the slope at the melting point. The value obtained in the liquid electrolyte for the polycrystalline electrode investigated is comparable to the average of the values obtained on single crystals seen in Figure 1.3 [48].

Markovic et al. [22] investigated hydrogen reactions at low temperature to obtain kinetic rates under slow reaction conditions. Here the temperature was varied in the range between 274 and 333 K. In other studies HER and HOR were investigated using a rotating-disk electrode (RDE) setup. Mass-transfer-corrected current densities of HER at 274 K are shown in Figure 1.14. In this approach the exchange current density was determined using micropolarization curves. Using only small overpotentials in

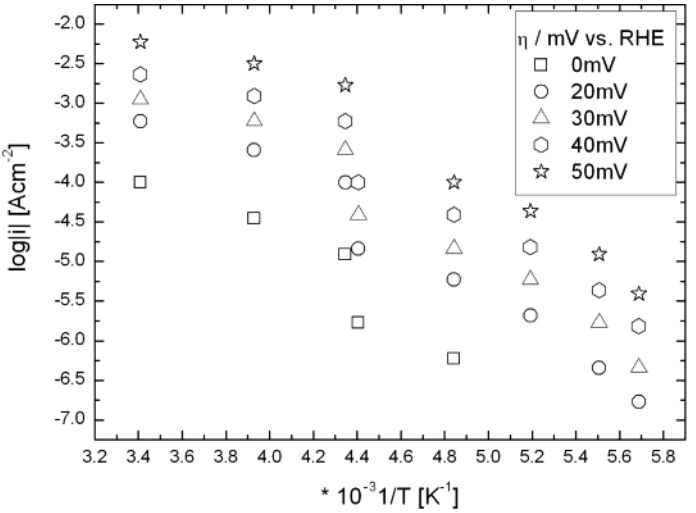

FIGURE 1.13 Arrhenius plot of polycrystalline Pt (Reproduced from Ref. 50.)

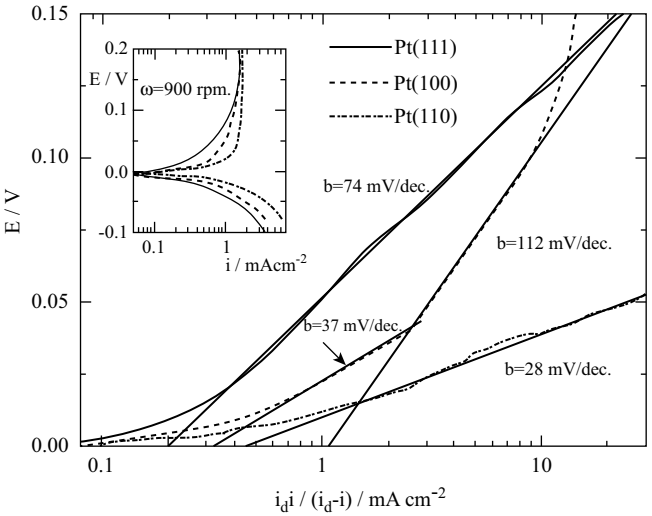

FIGURE 1.14 Tafel plots of mass-transfer-corrected currents for the HOR on Pt(*hkl*) in 0.05 M H_2SO_4 at 274 K. Inset shows polarization curves for HER and HOR at low overpotentials; rotation rate, 900 rpm [22].

the range of $\pm$ 10 mV versus the equilibrium potential, one can obtain a reliable value of j_0. Therefore the current potential curves were used to determine the slope from which the exchange current densities can be calculated. It was found that different single-crystal surfaces have different Tafel slopes and different exchange current densities (j_0). As was found before, the most reactive surface was Pt(110), with the lowest Tafel slope and the highest exchange current density. Interestingly, it was found that for low overpotentials the two branches of the Tafel plot are symmetric, as is shown in the inset of Figure 1.14. Hence, HER and HOR show the same exchange current density. It was added that the evaluation of exchange current density is more or less independent of the rotation speed. The values obtained by the micropolarization curves and the extrapolation in the Tafel plot to overpotentials equal to zero are in good agreement. It was also found that the activity has the same order, Pt(111) < Pt(100) < Pt(110), as mentioned above. At higher temperature the same results were obtained with higher net exchange current densities. The reactivity on Pt(*hkl*) single crystals can be summarized as follows. The reactivity was found to be strongly dependent on the crystallographic orientation of the single crystal. Whereas the activity represented by the exchange current density increases in the order of Pt (111) < Pt(100) < Pt(110), the activation energy decreases in the sequence $\Delta H_{(111)} > \Delta H_{(100)} > \Delta H_{(110)}$. Activity measurements show the same trend for different temperatures with different absolute values.

1.3.3 Au(*hkl*) Surfaces

As compared to platinum, gold is also not affected by air and water and hardly assailable by acids or alkalis. Au thin films on mica support are often used in

electrochemistry instead of single crystals with comparable results [52,53]. A thin Au film is evaporated on the mica with a very thin chromium interlayer to achieve a good adhesion. Flame annealing is a common procedure for preparing thin Au films and Au single crystals and leads to large (111) oriented terraces.

Cyclic voltammograms for Au(111), Au(100), and Au(110) surfaces in 0.1 M H_2SO_4 are shown in Figure 1.15 [27]. The investigations of sulfuric acid with the

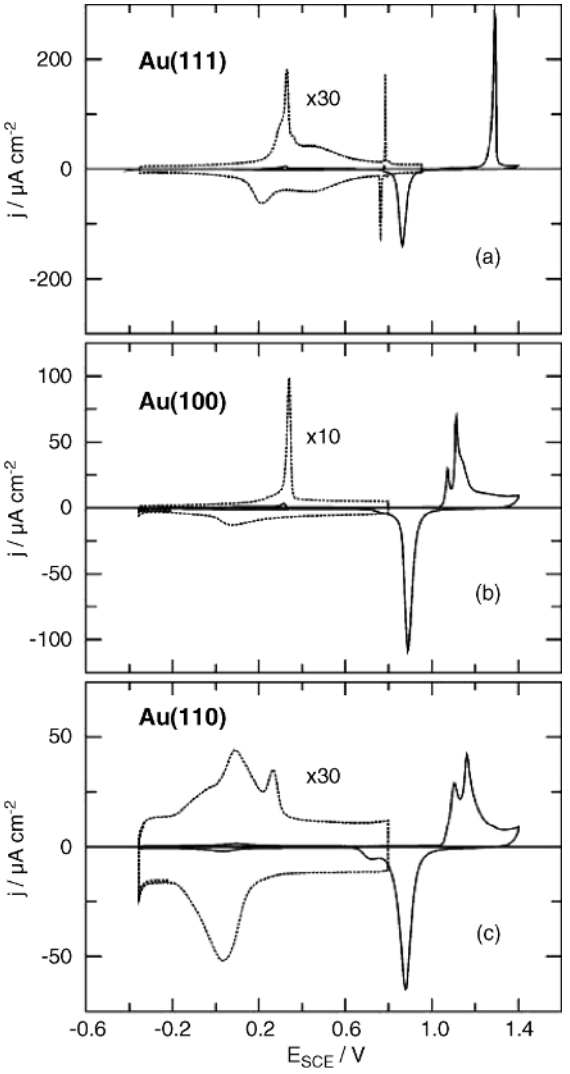

FIGURE 1.15 Cyclic voltammograms for Au(*hkl*) in 0.1 M H_2SO_4, scan rate 10 mV/s. The dotted curves are enlarged as indicated and represent the first cycles in the double-layer region, starting at −0.2 V [47].

typical current peaks in the voltammograms are especially indicative of single-crystal quality. Surface reconstruction of Au(111) and Au(100) is lifted at positive potentials of 0.34 V versus SCE due to adsorption of sulfate ions [54]. This leads to the unreconstructed (1×1) surface. Gold oxide formation begins at potentials higher than 1 V versus SCE. Because of the importance of Au(111) in electrochemistry as a support material, some important properties are summarized. Au(111) has several advantages, such as an easy preparation process and large potential window in the double-layer region. The quality of single-crystal Au(111) can be easily determined by cyclic voltammetry in sulfuric acid and evaluating the peaks attached to the lifting of reconstruction and forming ordered (v3xv7) $R19.1^\circ$ sulfate layer [47,55–57]. Defects as well as small terraces will inhibit the well-pronounced peaks at 0.34 V and 0.78 V versus SCE for the abovementioned procedures. Details on investigations on other low-index Au single-crystal surfaces can be obtained elsewhere [54,58–64]

Investigations of Au single crystals with respect to HER are quite rare [65–67] and show a weak dependence on crystallographic orientation in early studies. Comparable to Pt, precise investigations can be done only with high-quality single crystals and high standards for clean experimental conditions. Gonzales et al. [24] investigated the hydrogen evolution in different Au(*hkl*) single-crystal electrodes. To avoid a strong influence of adsorbing ions and to correlate the structure-sensitive reactivity to the different single-crystal electrodes, perchloric acid was used as electrolyte. Using a rotating-disk setup with hanging meniscus, concentration gradients of hydrogen at the interface were avoided. Results similar to those mentioned above for Pt crystal surfaces were obtained. Comparable to Pt, the different Au(*hkl*) surfaces are also structure-sensitive. Figure 1.16 shows that hydrogen evolution is obviously different

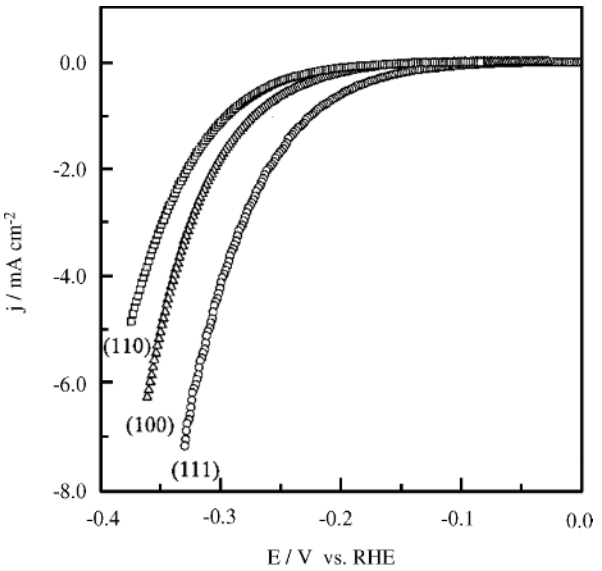

FIGURE 1.16 Polarization curves for hydrogen evolution on the low-index gold single-crystal electrodes in N_2-saturated 0.1 M $HClO_4$; sweep rate 10 mV/s, rotation rate 50 rpm [24].

on the three Au(111), Au(100), and Au(110) surfaces with respect to HER. With this result, it was proved that electrocatalytic activity is definitely dependent on the crystallographic orientation of Au single-crystal surfaces in the following sequence: Au(111) > Au(100) > Au(110). It was suggested that HER activity increases with the atomic density of the surface following the trend of increasing workfunction for the electron [68]. While the activity for hydrogen evolution is also dependent on the crystallographic orientation seen in the case of Pt, the measured net current densities are several orders of magnitude lower for Au.

1.3.4 Pd(*hkl*) Surfaces

Palladium, similar to gold and Platinum, is easily deformable and drawable to nearly any kind of profile such as gold and platinum. It is not affected by air and water but dissolves in oxidizing acids and molten alkalis. A unique property of Pd is the high hydrogen absorption ability, which may even change the lattice constant. This behavior complicates the preparation procedure because any kind of hydrogen during annealing would negatively influence the quality. Owing the hydrogen absorption into the bulk Pd, the hydrogen adsorption current region is superposed with the hydrogen absorption current in the cyclic voltammogram. To avoid this problem, thin Pd films that were epitaxially grown on supports such as Au(*hkl*) and Pt(*hkl*) were used to study hydrogen adsorption as well as hydrogen evolution and several other reactions [69–82]. As shown in Figure 1.17 for Pd(111), the potential window of the

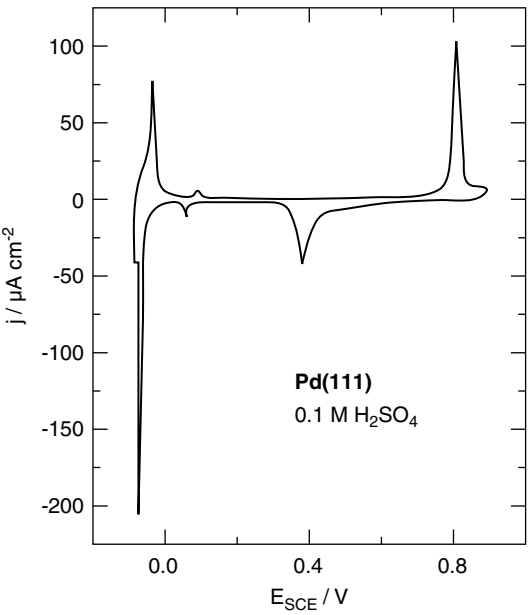

FIGURE 1.17 Cyclic voltammogram for Pd(111) in 0.1 M H_2SO_4; scan rate 10 mV/s [47].

double-layer region is large, and typical current peaks for hydrogen adsorption and oxide formation are pronounced. As mentioned before, Pd is often used as a thin film on different supports; hence the most experimental findings deal with Pd overlayers. Unexpected results for hydrogen reactions of thin Pd layers were obtained relative to electrocatalytic activity, and are reported in later sections

1.4 THEORETICAL STUDIES OF HYDROGEN CATALYSIS

1.4.1 Introduction

Computational methods such as density functional theory (DFT) or Monte Carlo simulations are powerful tools in surface science and catalysis. More recent improvements provide new insights in adsorption and desorption processes and reaction pathways. These results can be used to develop and design surfaces with specific properties such as new, more effective catalysts. Theoretical predictions often show good agreement with experimental results. Theoretical as well as experimental methods complement each other and therefore allow deeper insights and a comprehensive understanding that could not be explored with only one technique. Up to now theoretical quantum mechanical studies allow qualitative and sometimes even quantitative findings in surface science and catalysis and often play a leading role in new proceedings.

Principles of computational techniques and theoretical results are discussed in Section 1.4.2, The main focus is on the adsorption behavior of hydrogen and a theoretical explanation using the *d*-band center model. Pd on Au(111) is discussed as a special case in Section 1.4.3. This is followed by presentation of results from different theoretical groups from DFT calculations regarding hydrogen oxidation in Section 1.4.4 and the reaction pathway of hydrogen oxidation in Section 1.4.5. Calculations on metal surfaces and thin films of foreign metal on metal support is then reviewed and discussed in comparison to experimental findings.

1.4.2 Theoretical Fundamentals of Adsorption Behavior

One of the main objectives for surface scientists is to gain a fundamental understanding of the properties influencing the chemical reactions on surfaces. Hence, chemisorption of different reaction partners to the surface is important to access the abovementioned properties. More recent theoretical investigations show an appropriate, precise, and efficient trend to confirm the experimental results. The main focus is on hydrogen reactions, which are briefly discussed.

A theory of bonding adsorbates on transition metal surfaces was developed by Hammer and Nørskov [83]. In this model the chemisorption energy is determined by the interaction of adsorbate orbitals with surface *sp* and *d* bands. The model is simplified for atomic adsorbates, while the hybridization energy $E_{d\text{-hyp}}$ of the adsorbate with the metal *d* band can be calculated. Constant *sp*-band interaction energies imply that changes in $E_{d\text{-hyp}}$ on various metals are nearly identical to changes in the full

chemisorption energies E_{chem}. This leads to the conclusion that the Hammer–Nørskov model describes the changes in adsorbate chemisorption energies E_{chem} over different metals that are related to changes of the metal *d*-band centers. Thus the center of the *d*-band has a direct impact on the chemisorption energy E_{chem}. Chemisorption energies can be calculated quantitatively with this model, which is, for example, described in References 84–87. Next to the pure metal surfaces, pseudomorphic overlayers deposited on foreign metals also show a change in the chemisorption energies in theoretical calculations. Hydrogen chemisorption on Pd and Re single crystals as well as Pd and Re overlayers were investigated by Pallassana et al. [88,89]. A linear relationship was found between E_{chem} and metal *d*-band center ε_d. Besides adsorption energies, dissociation energies have also been calculated [83]. Summarized trends for chemisorption and thus, activity of well-defined metal surfaces and of overlayers on foreign supports can be calculated. Chemisorption energies and activation energies can be determined for different reactions and give trends for the catalytic behavior.

Next to the more general description of reactivity in terms of chemisorption and activation energy, several theoretical approaches for hydrogen reactions on various catalyst systems are given in the literature [87,90–100]. Hydrogen evolution as well as the hydrogen oxidation play an important role in electrochemical processes and technological applications [101–105]. It has been known for a long time that catalytic activity, which can be represented by the exchange current density plotted versus the hydrogen metal bond strength, is a volcano-shaped curve [106–109]. The shape of the curve is related to the Sabatier principle, which requires a moderate—neither too strong nor too weak—binding energy between surface and reaction partners [110]. Thus, the best catalyst should have intermediate binding energies to the educts as well as to the products. The free hydrogen adsorption energy ΔG_H is a reliable value for dissipating trends for hydrogen evolution [87,95,109]. Figure 1.18 [94] shows experimental values of exchange current density from the literature [87,95,109] plotted versus theoretical calculated values of ΔG_H. As can be seen, Pt, Pd, Ir, and Ru in the form of bulk crystals or as overlayers on foreign metals are near the top of the volcano curve. Their binding energy to hydrogen is neither too strong nor too weak, therefore yielding good catalyst behavior. Metals or bimetallic surfaces on the left side of the volcano curve bind hydrogen too strongly whereas metals on the right side bind hydrogen too weakly and thus are not adequate catalysts. Although there are some quantitative deviations between different experimental results, a clear trend is visible, which supports the qualitative volcano-shaped behavior. The most reactive catalysts for the hydrogen evolution lie on top of the volcano curve with $\Delta G_H \sim 0$, which is supported by experimental results showing Pt as the best pure metal hydrogen catalyst.

Nørskov et al. [94,96] investigated different alloys using DFT. The solute element was implemented in the host element, and the electrocatalytic properties were determined. It was shown that some alloys have a high degree of activity toward the hydrogen evolution, which is demonstrated by low ΔG_H values (indicated in dark red in Fig. 1.19). Therefore, ΔG_H can be used to quantify the hydrogen metal bond strength; values of $\Delta G_H \sim 0$ lead to high HER activity [87]. For this high-throughput method, used to determine catalysts for hydrogen evolution binding energies, activation barriers, preexponential factors, and other parameters were considered. In this

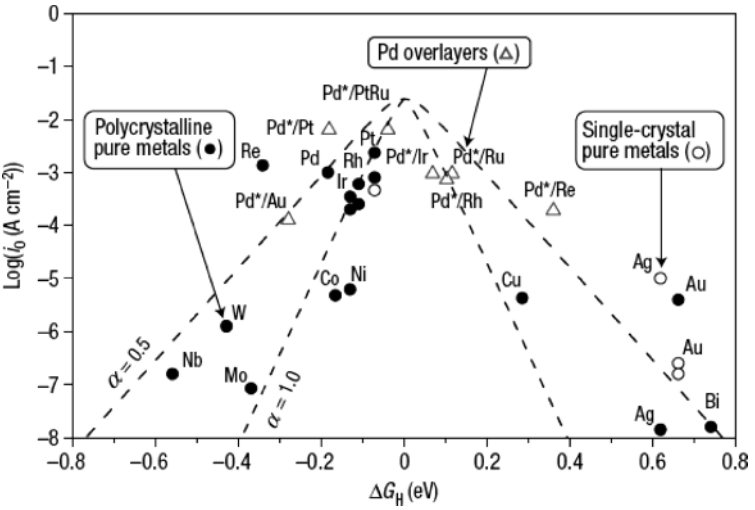

FIGURE 1.18 Volcano plot for the HER for various pure metals and metal overlayers. ΔG_H values are calculated at 1 bar of H_2 (298 K) and at a surface hydrogen coverage of either $\frac{1}{4}$ or $\frac{1}{3}$ML (i.e., one-fourth or one-third of a monolayer). Experimental data were compiled in the literature [87,95,109]. Where available, computational data are taken from the present work; other computational results are taken from the three references cited above. The experimental data were collected from over 40 years of publications, representing different experimental conditions and surface structures. No corrections for changes in the calculated ΔG_H values with coverage are included, in contrast to the calculated values for Pd overlayers (denoted by Pd*/substrate) presented by Greeley et al. [95]. The two curved lines correspond to the activity predictions of simple mean-field, microkinetic models, assuming transfer coefficients (a) of 0.5 and 1.0, respectively [12].

case the reduction of protons and the removal of adsorbed hydrogen are balanced. DFT calculations [96] have already shown their power to predict a high activity that is supported by experimental results [94,95]. Hydrogen-binding energies for several bimetallic systems are shown in Figure 1.19. Metal alloys have been evaluated by DFT calculations and were presented in a matrix format. Different promising catalyst systems can be selected and discussed in detail, but instead an overview of trends gleaned from single investigations on several promising candidates should be given. In principle, it can be shown that low solute metal coverages of late-group transition metals have high ΔG_H values. For early-group metals the opposite trend was found, with free energy decreasing from lower right to upper left of the small matrix inset. These findings are in line with the Hammer–Nørskov model [111,112]. Interestingly, all alloys with Pt, Pd, or Ru are highly active toward hydrogen evolution. Almost all combinations with these three metals as host as well as solute element have ΔG_H values close to zero. These three metals were also found to be the best catalysts for HER in the Nørskov et al. [87] study, where pure elements were investigated. An astonishing result is that the behavior of a full monolayer of solute metals (shown in Fig. 1.19c) behaves differs from that of a third or two-thirds monolayer.

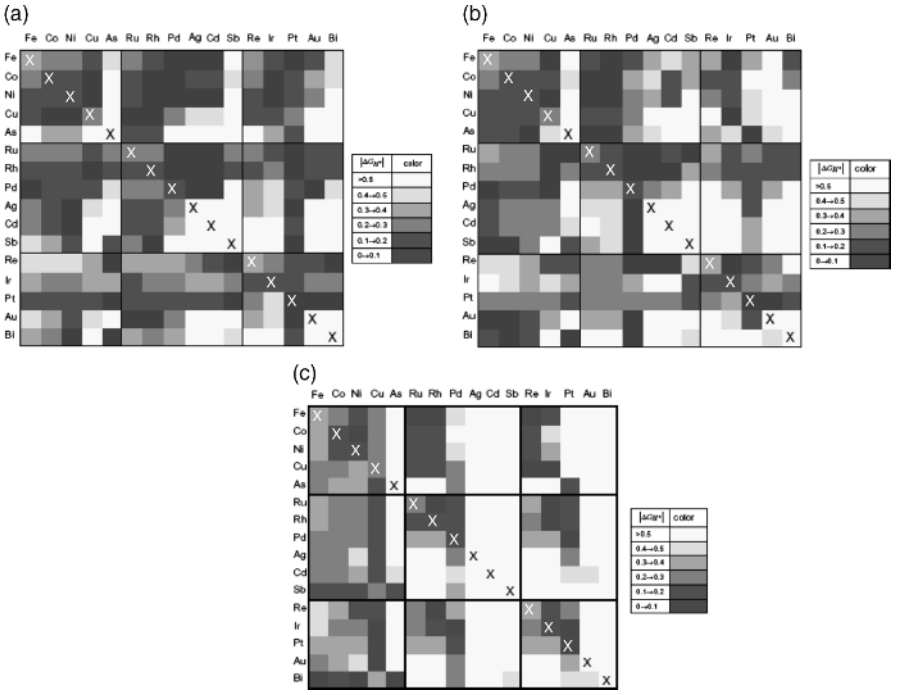

FIGURE 1.19 Magnitudes of free energies of hydrogen adsorption ($|\Delta G_H|$) at $T = 298$ K, $\theta H_{\frac{1}{3}}^{1}$ ML. All free energies are referenced to gas-phase H_2. Coverage of solute elements (columns) in the surface layer of host elements (rows) is (a) $\frac{1}{3}$ ML, (b) $\frac{2}{3}$ ML, and (c) 1 ML. The X symbols (tickmarks) on diagonals denote pure elements [96].

This would indicate that submonolayers of solute elements are more reactive than are full monolayers. It was suggested that these findings are due to a strain effect in the lattice constant that strongly influences ΔG_H and thus, the behavior toward the activity [85]. Although many very promising candidates for catalysts for HER have been presented, only a few are stable under electrochemical conditions. Out of these 768 possibilities, only 30 were predicted to be stable, as they often contain Rh, Ru, Pt, Pd, and Ir, which are known to be active. Other promising candidates containing Rh, As, and Re have to be validated by experiments.

1.4.3 Hydrogen Adsorption on Pd Monolayers on Au(111)

After a general overview of chemisorption and adsorption of hydrogen on various metals, a special case is presented in this section. Theoretical calculations of the hydrogen adsorption on Pd on Au(111) [91,92,113] are discussed. Figure 1.20 [113] shows the hydrogen adsorption energy versus the number of Pd overlayers on Au(111) is shown. For comparison, pure Pd is also given on the right side of the figure. According to calculations of lattice constants of Au (4.18 Å) and Pd (3.96 Å), the Pd overlayer is strained by $\sim 5\%$. This expansion leads to higher binding energies of

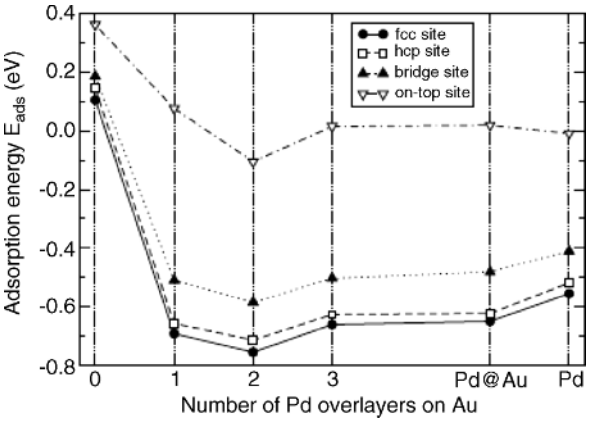

FIGURE 1.20 Atomic hydrogen adsorption energies as a function of the number of Pd overlayers on Au(111) for different adsorption sites on the (111) at a coverage of $h = 0.25$. The pure Pd substrates with the lateral lattice constant of Au ($a = 4.18$ Å) and Pd ($a = 3.96$ Å) are labeled by Pd@Au and Pd, respectively [113].

hydrogen on Pd according to the *d*-band model. Interestingly, the adsorption energies for one and three monolayers of Pd on Au(111) are similar and do not differ much from those for bulk Pd. Thus, it was suggested that a strain effect due to the support is limited to layers of only a few monolayers' thickness. An unexpected result is that the adsorption energy is maximized for two monolayers of Pd on Au(111), which is due to an extreme position of the *d*-band center. This was explained with the assumption that for only one Pd monolayer, some indirect interactions between the adsorbate and Au(111) influence the activity. This effect is negligible for two monolayers. These results might have to be extrapolated from the solid–vacuum interface to the solid–liquid interface, which requires several modifications. One of the most important issues is the presence of water adlayers on the electrode [114–116]. For less reactive surfaces the water adlayers remain unaffected on the surface and form a stable overlayer. This will change if the surface is reactive and the water may partially dissociate. Although there is an influence of the water adlayer the hydrogen binding energy is reduced by only 100 meV. Because of this weak interaction of water with Pd on Au(111) there will not be a significant influence on the water adlayer. Therefore, it can be concluded that studies at the solid–vacuum interface can give reliable values as well as trends for the adsorption of hydrogen at the solid–liquid interface.

1.4.4 Theoretical Fundamentals of HOR

The hydrogen oxidation reaction has been intensively investigated because of its importance in electrochemistry. Interestingly, the rate of hydrogen oxidation varies for different metals over six orders of magnitude. Metals such as mercury have a very slow hydrogen oxidation rate, whereas platinum is highly reactive toward HOR. As mentioned above, the catalytic activity of different materials can be correlated to the

workfunction [109], metal hydrogen bonding [87], and the unfilled *d* orbital [117]. More recently developed concepts for gas-phase catalysis were discussed above and mainly in regard to the position of the *d*-band center [90]. The results from gas-phase catalysis calculations can be extrapolated to electrocatalysis, considering important issues such as the interaction with the water adlayer or the solvent. For hydrogen oxidation, a hydrogen molecule is oxidized in two protons and two electrons, whereas the protons are stabilized by a solvent. The electrons are transferred to the metal and the solvated protons desorb into the solution, which will result in a relaxed system [99]. This is induced by lowering the energy of the system when the bonding orbital passes the Fermi level. Santos and Schmickler [98] state that it is important to exercise caution when employing several procedures occurring in the electrochemical environment. As mentioned above, the interaction between water and the proton is very strong; hence, the water molecules have to be considered in the calculations. Furthermore, the electrode potential has not been introduced in the calculations. Additionally, it is not yet possible to consider the solvent fluctuations that change the electronic level past the Fermi level. Different approaches were used to develop a model that accounts for breakage of the electrochemical bond, which was suggested to explain a possible lowering of the activation energy. An important aspect is the interaction of the metal with reaction partners. Therefore, chemisorption, which depends on electronic energy, is of fundamental interest. The chemisorption energy function can thus be calculated and can be used to determine the trend of hydrogen activity for different metals. Up to now it has not been possible to calculate exact values because of insufficient accuracy of available experimental values in the calculation. However, a trend can be established with relative values to estimate whether a catalyst will show good catalytic behavior toward hydrogen oxidation. Santos and Schmickler [98] calculated potential energy surfaces of the bond length between two hydrogen atoms and the generalized solvent coordinate q, which corresponds to the solvent configuration. A neutral hydrogen molecule has a solvent coordinate of $q = 0$, whereas two protons have a solvent coordinate of $q = -2$. Figure 1.21 shows two potential energy surfaces for two different catalysts. As can be seen, the reaction pathway starts in a valley where a hydrogen molecule goes through a saddle point and ends in a valley where two protons as reaction products are located. The activation energy determines the saddle point of the curve that has to be conquered. It is obvious that in the case of platinum in Figure 1.21 (c,d) the activation energy is lower than that for *sp* metals (in Fig. 1.21a,b). This leads to the assumption that desorption of hydrogen is the rate-determining step, and not the bond breakage of the hydrogen molecule. Comparing the calculations with different experimental values is a difficult task because of the wide scattering of these values. Different experimental techniques as well as a difficult electrode preparation leads to inconsistent findings. Therefore, it was suggested that the higher measured activity seems to be the most reliable, due to inhibiting effects caused by contamination and slow measurement techniques. Despite these discrepancies in theoretical and experimental values, the theory yields a successful prediction of powerful catalysts.

It can be concluded that two concepts have to be considered: (1) the metal–hydrogen interaction explained by the *d*-band center model and (2) the reaction pathway determined by the strength between the metal and the molecule.

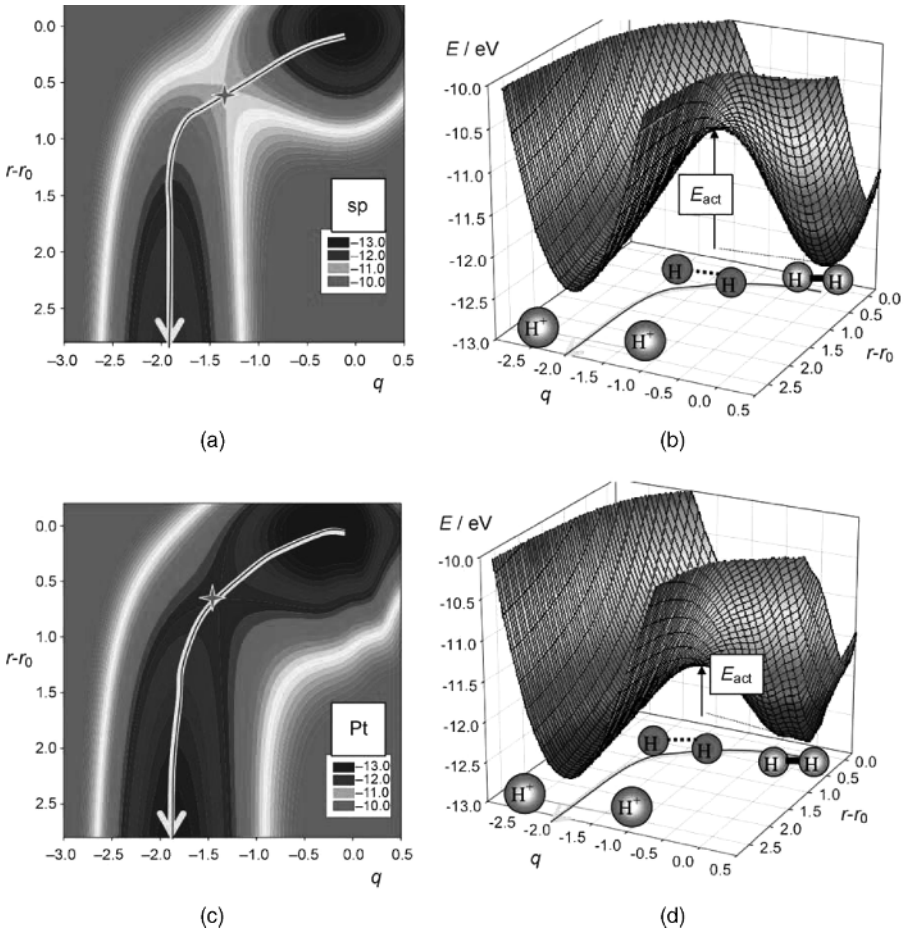

FIGURE 1.21 Potential-energy surfaces for oxidation of H_2 as a function of bond length r and solvent coordinate q. The equilibrium bond length is denoted by r_0; r is given in atomic units (1 au = 0.529 Å). (a,b) *sp* metal; (c,d) platinum. The red crosses denote the saddle points [98]. (See insert for color representation.)

1.4.5 Theoretical Model of Spillover Concept for HER

Eikerling et al. [93] developed a kinetic model of the hydrogen evolution on single Pd particles supported on Au(111). This model is able to explain the experimental finding from STM investigations of Meier et al. [118]. It was shown that hydrogen desorption from Pd surfaces is the rate-determining step. If the desorption is small, adsorbed hydrogen can spill over from the catalyst particle to the Au surface, which acts as hydrogen storage. The principal mechanism of the hydrogen spillover model is shown in Figure 1.22, and the steps are described as follows: (1) the solvated protons diffuse through the electrolyte to the catalyst particle, (2) charge transfer occurs at the catalyst particle and the proton will be reduced to adsorbed hydrogen H_{ad}, (3) H_{ad} diffuses on

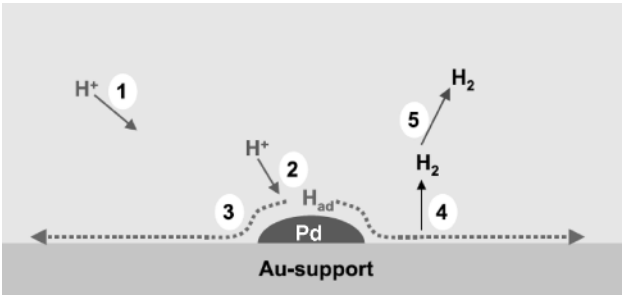

FIGURE 1.22 Illustration of the processes on the substrate surface involved in the reduction of protons: (1) bulk diffusion of protons, (2) proton discharge and formation of adsorbed hydrogen, (3) spillover and surface diffusion of adsorbed hydrogen, (4) recombination and desorption of molecular hydrogen, and (5) hydrogen diffusion in bulk electrolyte [11].

the Pd particle and spills over to Au(111) support, (4) recombination of two adsorbed hydrogen atoms to an adsorbed hydrogen molecule $H_{2,ad}$ and subsequent desorption of the $H_{2,ad}$ occur, and (5) H_2 diffuses in the electrolyte.

It was shown that the diffusion of hydronium ions is much larger for small particles compared to flat surfaces, due to hemispherical diffusion. The diffusion-limiting current can be up to 5×10^5 A/cm^2 for particles of radius 2 nm and a proton concentration of 10^{-4} mol/cm^3. The experimental setup with an STM tip as local sensor allows elimination of the diffusion limitation due to the small current. Therefore, it can be estimated that the proton discharge and the adsorption at Pd are the rate-determining steps. It was concluded that desorption rates of adsorbed hydrogen on the Pd particle are small and the enhanced current densities can be explained by a hydrogen spillover to the Au surface. For particles with a height of one or two monolayers, turnover rates and small desorption rates were found. The adsorbed atomic hydrogen will expand in diffusion fronts on the Au support and will recombine to hydrogen molecules and subsequently desorb. Larger particles behave in a different way. Their electrocatalytic activity is about two orders of magnitude lower compared to small particles. This means that hydrogen spillover is therefore reduced. This behavior can be explained by an upshift of the *d*-band center and hence a weaker hydrogen bonding to the Pd, which was described by the model of Hammer and Nørskov [83,90]. The spillover model is in good agreement for the hydrogen evolution from experimental work and can be supported by theoretical models. Up to now it has been difficult to apply the same model for the reverse hydrogen oxidation reaction.

1.4.6 Summary and Discussion

Modern theoretical approaches provide powerful and fast tools for investigation of fundamentals at the solid–vacuum interface. Comparison with electrochemical experiments indicates that the trends and results are also applicable to the solid–liquid interface and hence to electrochemical issues. Hence chemisorption, adsorption and

reaction pathway calculations can be used to gain deeper insights in and improved understanding of fundamental reactions. These findings can be used to determine or modify certain properties and also to systematically enhance the catalytic properties. With modern approaches by theory, findings can be explained more accurately or even predicted. This allows the development of promising catalyst systems to be investigated and proved in a systematic stepwise fashion by experimentalists, which has been shown to be fruitful in more recent studies. Theoretical catalysis on pure metal as well as metal overlayers on foreign substrates has been introduced. Interesting und unexpected results were extracted and will serve as a background for future experimental results.

1.5 FUNDAMENTAL STUDIES OF NANOPARTICLES ON SINGLE CRYSTALS

1.5.1 Introduction

Small nanostructures and nanoparticles of different materials often show properties different from those of bulk material. Since platinum and palladium are two of the most important catalysts for hydrogen reactions, they have been intensively investigated. The scientific focus is on fundamental processes and reaction mechanisms occurring at these reactive materials, especially their electrocatalytic activity. The reactivity of the catalyst can be influenced by several variables, such as particle size and particle distribution, influence of the support, and the ratio between low and high coordinated atoms of the catalyst. Scientists have already achieved a closer look into the fundamentals of hydrogen reaction, which also allows improvement of catalyst behavior. Therefore, much experimental as well as theoretical work performed to further understand the hydrogen reaction mechanism on well-defined catalyst surfaces was reviewed in Sections 1.3 and 1.4. A special case occurs if Pt and Pd are deposited onto foreign metal supports. Due to lattice strain of the Pt or Pd overlayer, the reactivity toward the hydrogen reactions differs from that of the bulk material. Many experimental studies on monolayers and submonolayers of metals on foreign metal substrates have been performed with interesting findings. However, a complete understanding that describes the overall effect has not been found until now. This section reviews the results on electrocatalytic activity of Pd and Pt multilayers, monolayers, and submonolayers on different single-crystal surfaces and compares them with those for bulk material. The different surfaces were investigated with respect to their electrocatalytic properties toward HER and HOR using various electrochemical methods. Section 1.5.2 describes the behavior of Pd overlayers on different supports. Adsorption and desorption behavior as well as the electrocatalytic activity toward hydrogen reactions of Pd overlayers are described. Investigations of Pt overlayers on Au(111) are shown afterward, followed by a summary and a discussion of all work presented thus far. More recent statements are combined and may provide some new insights into the understanding of different properties influencing activity related to hydrogen reactions.

1.5.2 Pd on Single-Crystal Surfaces—Adsorption/Absorption/ Desorption of Hydrogen

Palladium deposition was studied regarding deposition mechanisms [119–126] for different metals. Bimetallic electrodes consisting of various metal supports and Pd overlayers have several advantages, such as the relatively easy preparation and well-established electrochemical treatment. By contrast, Pd single-crystal preparation is elaborate because of the necessary absence of hydrogen. Also, the hydrogen absorption into the Pd single crystal must be considered since it can negatively affect the quality of the single crystal. In most cases except for Au(111), Pd grows in one complete monolayer and continues growing in a three-dimensional mode [127]. Pd on Au(111) can grow two-dimensionally in up to two monolayers [119], which is ideal for further investigations. Because of the support, the Pd monolayer behaves differently than bulk Pd. It was shown by Kolb is group [121,127,128] that the adsorption and desorption properties of thin Pd overlayers change with respect to the Pd bulk material. Early studies [128] showed that with increasing Pd overlayer thickness on Au(111), the adsorption behavior of hydrogen approaches that of bulk properties of palladium. This was explained by a change in the lattice of the Pd overlayers due to the Au(111) support material. With increasing thickness of the Pd overlayer on Au(111), the behavior approaches that of Pd(111) massive crystal, indicating the importance of the support. In a study by Kibler et al. [127] on Pd monolayers on different supports, different reaction rates due to lateral strain effects were shown. Several metal electrodes such as Au(111), Re(0001), Ru(0001), Rh(111), Ir(111), Pt/Ru(111), and Pt(111) were used to electrochemically deposit palladium monolayers. The effect on hydrogen adsorption and desorption was investigated. The decorated Pd metal electrodes have different binding energies of Pd to hydrogen caused by the support, as shown in Figure 1.23. Baldauf and Kolb [121] showed that thin Pd overlayer shows a high overpotential for hydrogen absorption. Thus, small hydrogen adsorption currents can be resolved that are typically superposed by absorption currents. Cyclic voltammograms for different Pd metal electrodes are shown in Figure 1.23 [127]. For comparison, a Pd(111) single crystal is also added. Only the Au(111) support has a peak potential that is more positive than that of pure Pd(111). All other supports desorbed hydrogen at much lower potentials compared to palladium. It was suggested by the author that these peaks can be an indicator for the adsorption strength of hydrogen to the metal.

Comparing the results from Figure 1.23 with theoretical calculations from Nørskov et al. [129,130], we see an indicator of direct impact onto the binding energies. The shift of the *d*-band center of Pd overlayers on different supports was calculated assuming the simple model shown in Figure 1.24a. Pd is indicated in the figure, and the Pd atoms are relaxed in the bulk material. Using another support changes the lattice constant of the Pd overlayers and induces a positive or negative strain. It is also shown that a change in the lattice constant affects the *d*-band center in the metal. Figure 1.24b shows the peak potential of the electrode versus SCE for the hydrogen desorption for Pd monolayers on different foreign metal supports. The electrode potentials are plotted versus the *d*-band center shifts from the study by Ruban et al. [130] following a

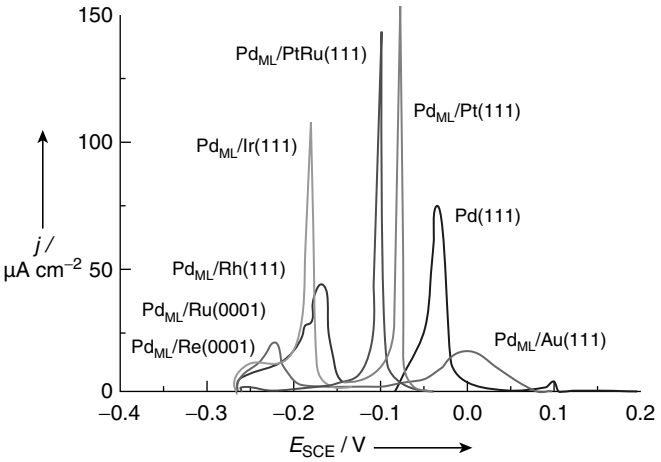

FIGURE 1.23 Positive voltammetric sweeps for Pd(111) and pseudomorphic palladium monolayers (PdMLs) on seven different single-crystal substrates in 0.1 M H_2SO_4, revealing a spectrum for hydrogen desorption. Scan rate $v = 10$ mV/s [127].

linear behavior. Kibler et al. [127] showed that the change in electronic behavior of Pd monolayer has two contributions: (1) the lattice constant of the overlayer changes with the different lattice constant of the support and thus induces a shift in the *d*-band center (geometric effect) and (2) there is also a so-called ligand effect that is also caused by a change of the *d*-band center if there is a large electronic interaction between the surface layer and the substrate. However, the systematic change of the *d*-band center leads to the conclusion that the geometric effect is the controlling one. These findings may give rise to the conclusion that changed adsorption behavior due to lattice mismatches will also result in changed reactions or kinetic properties.

1.5.3 Pd on Au(111)—HER and HOR

The hydrogen evolution reaction was investigated on Pd deposited on Au(111), and several effects were found for single Pd particles [131–133] as well as large Pd nanostructured Au(111) electrodes [134,135]. Nanoscale effects such as spillover of hydrogen as well as geometric effects can influence the reactivity of Pd supported on Au(111) toward HER. As mentioned in Section 1.5.2, the geometric effects change the binding energy to hydrogen. This effect is due to a strain of the overlayer caused by the support, which has a different lattice constant. This effect was also found from theoretical calculations [127,136–140]. Pandelov and Stimming [134] investigated monolayers and submonolayers of Pd deposited on Au(111) with respect to HER. The Pd overlayer thickness was lowered from four monolayers to about 3.5% of a monolayer, causing an increase of about one order of magnitude for the geometric current density. It was shown that the geometric current density increases with decreasing palladium coverage, as shown in Figure 1.25. The strong enhancement in the case of submonolayers was explained by a hydrogen spillover from the Pd

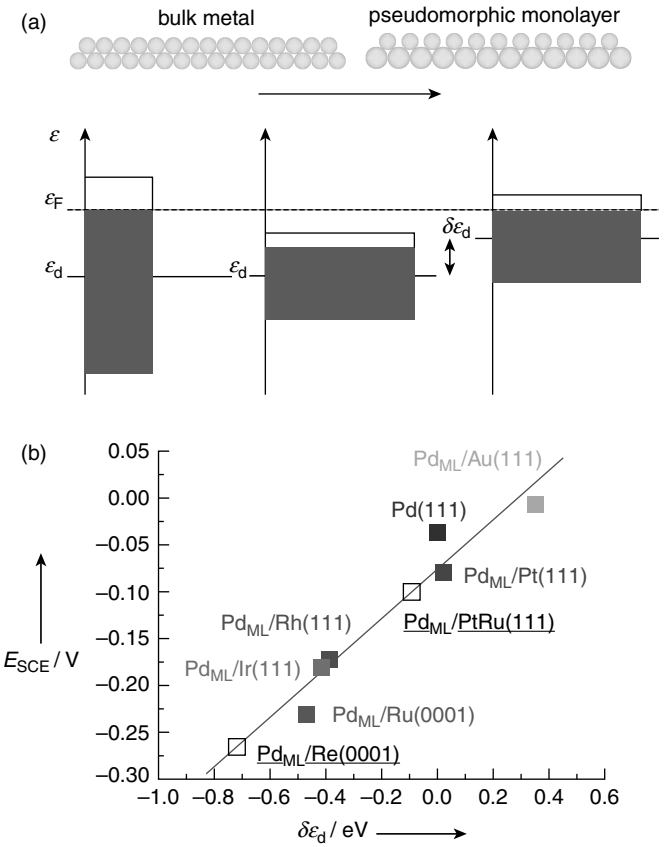

FIGURE 1.24 (a) The main origin of a shift in the *d*-band center ε_d is a change in the interatomic distances within an overlayer. If the *d* band of a metal is more than half-filled, an expanded pseudomorphic monolayer will lead to an upshift of ε_d owing to band narrowing and energy conservation [131]. (b) A plot of the hydrogen desorption potentials versus the shift of the *d*-band center, $d\varepsilon_d$ shows a linear correlation as theoretically predicted [131]. For palladium on the Re(0001) substrate, no hydrogen peak was measured (see text). The hydrogen peak at −0.1 V for palladium on PtRu(111) suggests a shift of the *d*-band center $d\varepsilon_d$ of about −0.1 eV, which has not yet been calculated [127].

catalyst particle on the Au(111) surface. This result indicates that with lower amounts of noble metal, a higher net activity is possible, which is in clear contrast to expectation.

Referring to the current values per active palladium area, a very strong increase in activity with decreasing coverage (Fig. 1.26) is found. Almost three orders of magnitude enhancement in activity comparing four monolayers of palladium with only $\sim$ 3.5% Pd on Au(111) were determined for two different overpotentials. Different explanations were discussed, whereas no dependence of the current density on the number of edges versus terrace atoms could be found as proposed by Meier

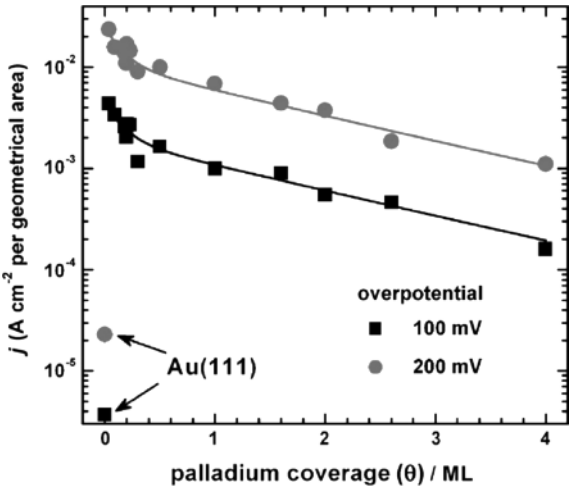

FIGURE 1.25 Current density of hydrogen reduction as a function of the Pd coverage at 100 and 200 mV overpotential, respectively. The current densities were calculated with respect to the geometric electrode area. The bulk symbols are the measured values, and the solid-line curves are for visual inspection [134].

et al. [132]. While the increasing reactivity for monolayers can be explained by the strain effect in the palladium lattice, the increase for submonolayers of Pd was explained by a spillover mechanism of reaction intermediates. This suggests a direct contribution of the support in the hydrogen evolution.

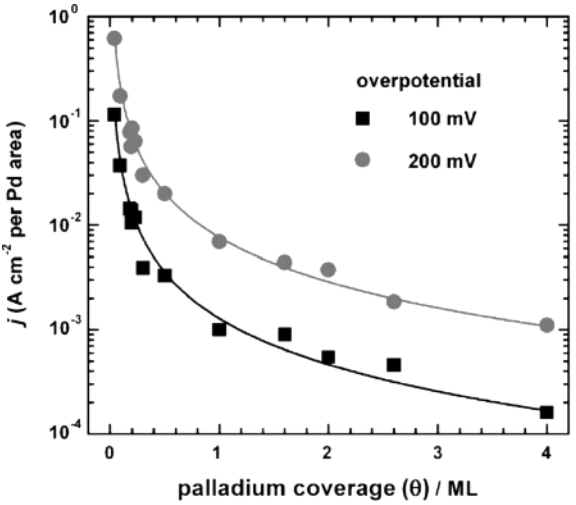

FIGURE 1.26 Current density of hydrogen reduction as a function of the Pd coverage at 100 and 200 mV overpotential, respectively. The current densities were calculated regarding the Pd area. The bulk symbols are the measured values and the solid curves are a guide for the eye [134].

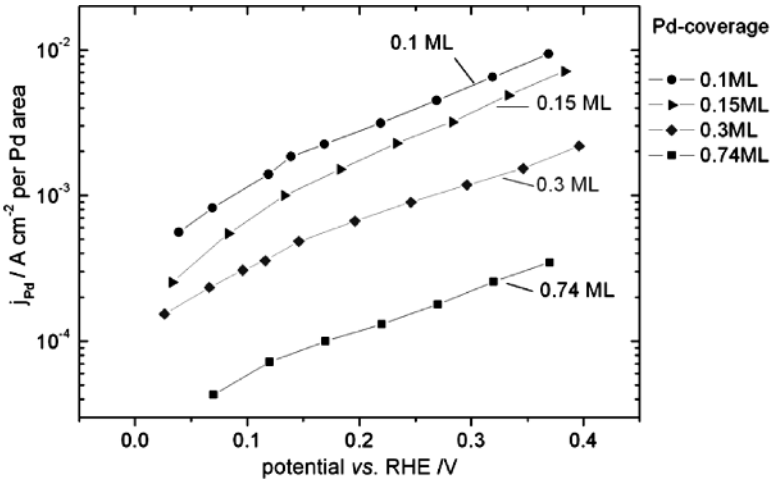

FIGURE 1.27 Electrocatalytic activity of HOR per Pd area of the Pd/Au(111) system in 0.1 M $HClO_4$. The current density is normalized to the surface area of the deposited Pd [141].

Similar results were found by Wolfschmidt et al. [141] for HOR. A decreasing coverage of Pd on Au(111) shows an increase in the absolute current densities. Referring these values to the active Pd area, a strong enhancement of the specific catalytic activity is found, as shown by Pandelov and Stimming [134] before. In Figure 1.27 the specific current densities for HOR are about two orders of magnitude higher on comparison of 0.74 ML with 0.1 ML of Pd deposited on Au (111). These findings were explained with altered electronic structure of the Pd overlayer. With the shift in the *d*-band center the binding energy to hydrogen is changed and thus can enhance the reaction. The latter explanation is valid for multilayers down to one monolayer and not directly applicable to the case of submonolayers. A spillover model comparable to HER has been considered in the context of a more complex theory. The influence of reactive steps and defects cannot be excluded but does not seem to be an important factor. It is a major challenge to find a general mechanism for HOR on submonolayers.

1.5.4 Pd on Pt(111)

Markovic and Ross [142] performed experiments on Pd films on Pt(111) and compared the activity for HER and HOR to the activity of a Pt(111) single crystal. Comparison of pure Pt(111) with a Pd-modified Pt(111) single crystal shows an enhanced reactivity that is clearly seen in Figure 1.28. The catalytic activity for hydrogen reactions was investigated with a RDE at a rotation speed of 1600 rpm. The Arrhenius plot inset in Figure 1.28 shows that the activation energy for hydrogen reactions is only half that for the Pt(111)–Pd electrode compared with Pt(111). For the so-called paradoxical activity of the Pt(111)–Pd surface for HER and HOR, it is important to understand the nature of H_{upd} and the effect on H_{opd} formation. The authors suggested that the

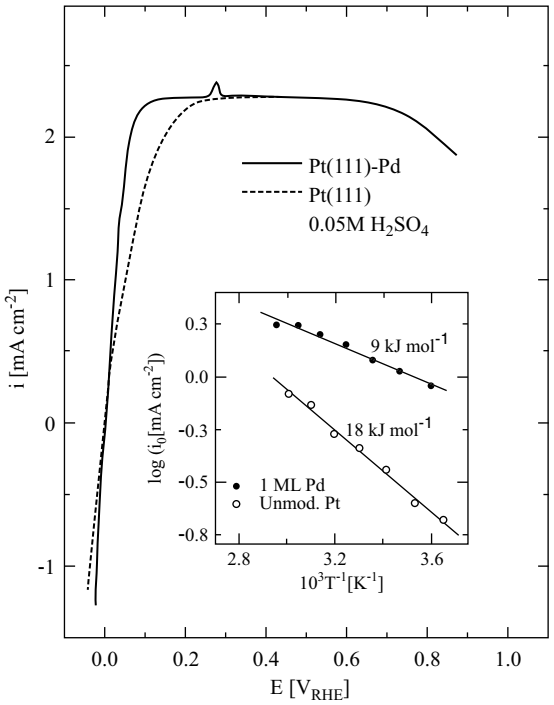

FIGURE 1.28 Comparison of the HER/HOR on Pt(111)–Pd (solid-line curve) and Pt(111) (dashed-line curve) in 0.05 M H_2SO_4 at 278 K. Rotation rate 1600 rpm [inset: Arrhenius plots for HER/HOR on Pt(111)–Pd and Pt(111)] [25].

transition of unreactive H_{upd} into reactive H_{opd}, due to high coverages of H_{upd} on Pd/Pt(111), seems to be reasonable. However, it seems uncertain whether the change in adsorption energy has an important role in the enhanced electrocatalytic behavior for the Pd/Pt(111). The importance of the altered adsorption energetics of hydrogen due to electronic effects on Pd on Pt(111) support in contrast to the pure Pt(111) were emphasized later. It was concluded that the electronic effects play an important role in electrocatalysis.

The influence of Cu, Pb, and Bi on the reactivity of different Pt(*hkl*) single-crystal surfaces was also investigated by Markovic and Ross [142]. In these investigations Cu and Pb were deposited as an underpotential monolayer and Bi was deposited as irreversible uncomplete monolayer. Because of overlap of the metal deposition and hydrogen evolution, only hydrogen oxidation was investigated. All metal modified Pt surfaces inhibit the HOR compared to pure Pt(111) surfaces, which is shown in Figure 1.29. These modifications of the Pt surface with overlayers of foreign metals did not result in improvement of the catalytic properties. But some interesting conclusions can be drawn from these inhibiting effects. The activity toward the different overlayers can be expressed as Bi > Pb > Cu deposited on Pt(111). The highly active Bi overlayer becomes less active at higher overpotentials, due to adsorbed OH on adjacent Pt sites.

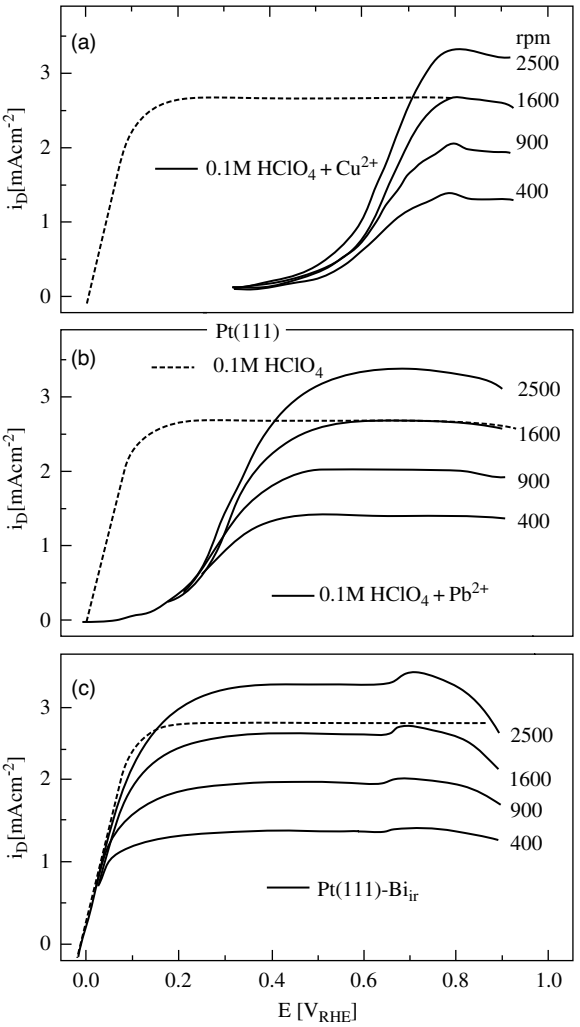

FIGURE 1.29 (a-c) Polarization curves for HOR on Pt(111) in 0.1 M $HClO_4$ (dotted-line curve), recorded at 1600 rpm. (a) HOR on Pt(111) in 0.1 M $HClO_4 + 10^{-3}$ M Cu^{2+} (solid-line curve) at sweep rate 20 mV/s; (b) HOR on Pt(111) in 0.1 M $HClO_4 + 10^{-3}$ M Pb^{2+} (solid-line curve) at sweep rate 20 mV/s; (c) HOR on Pt(111) in 0.1 M $HClO_4$ (dotted-line curve), and on a Pt(111)–Bi_{ir} electrode in 0.1 M $HClO_4$ at sweep rate 20 mV/s [24].

It is suggested that the free Pt sites play a major role for the strong HOR activity in the Bi case. In contrast, Pb and Cu metal adlayers do not influence the energetics of the absorbed hydrogen, but they block the free available Pt sites. The low activity of the Cu-modified Pt(111) surfaces was explained by the strong adsorption of anions, which has a significantly negative influence on HOR.

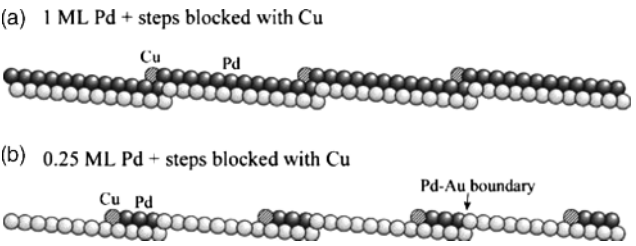

FIGURE 1.30 Hard-ball models of a Au(665)/Pd electrode where the Pd step sites have been blocked by Cu, modified with (a) 1 ML of Pd and (b) 0.25 ML of Pd [144].

1.5.5 Pd on Au(111)—Blocking Active Sites with Cu

Palladium on Au(111) was intensively investigated by the Baltruschat group [144–146]. Different single-crystal surfaces such as Au(111), Au(332), and Au(331) were decorated with Pd to investigate their properties regarding the adsorption of hydrogen. It was found that it is necessary to deposit more than one atomic row of Pd onto the stepped Au surfaces to adsorb hydrogen [145]. Further findings on Au(332)- and Au (665)-decorated single crystals show a strong influence of the steps on the catalytic activity toward hydrogen evolution. This is in line with the findings on the weak hydrogen adsorption according to the Sabatier principle. An interesting effect was found by blocking the active Pd rows on the different stepped Au surfaces with Cu, schematically shown in Figure 1.30. Regarding Pd/Au(665) with Pd steps blocked by Cu, the electrocatalytic activity decreases to values that are in the order of magnitude of a Au(665) covered with more than a full monolayer of Pd. It was concluded that hydrogen spillover seems unreasonable for Pd-covered surfaces, which is in contrast to findings by the Stimming group [134,141,147]. Regarding hydrogen evolution and oxidation, it was found that below one monolayer of Pd on Au(332) the reactivity is independent of coverage. Therefore, it was deduced that the reactivity is caused mainly by the step sites and that contact between the Au and the Pd atoms is necessary. The effect of Pd deposited on terraces is negligible. Furthermore, it was concluded that Cu is able to block the active Pd rows on stepped Au surfaces and hence, to decrease the activity of the Pd atoms regarding hydrogen evolution.

1.5.6 Pt on Au(111)

Platinum-modified Au(111) surfaces were investigated by Wolfschmidt et al. [141] in terms of their electrocatalytic properties for HER and HOR. Several scanning tunneling microscopy (STM) images of the investigated nanostructured electrodes are shown in Figure 1.31. Different methods such as integrating the deposition charge, hydrogen underpotential deposition, CO monolayer oxidation, and STM were used to determine the amount of deposited metal. Comparing the different methods allows a detailed and precise access to the exact amount of Pt.

It was shown that monoatomically high Pt islands on Au(111) have a strongly enhanced catalytic activity for both hydrogen reactions. The kinetic current densities

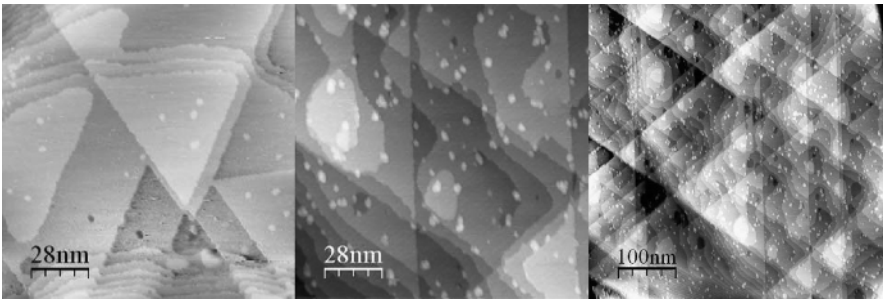

FIGURE 1.31 STM images of different Au(111) electrode surfaces nanostructured with Pt. The images were recorded in air with $U_{bias} = 100\,mV$ and $I_T = 1\,nA$. The amount of Pt on Au(111) corresponds to (a) 0.025 ML, (b) 0.067 ML, and (c) 0.13 ML of Pt [141].

are shown in a Tafel plot in Figure 1.32. It is obvious that the Pt(111) single-crystal electrode has the highest reactivity for both reactions referred to the simple geometric electrode area. A clear trend toward their electrocatalytic activity for the different amounts of Pt on Au(111) was not found for the geometric current density. Although the activity of the submonolayers is less than the activity of the Pt(111), it can already be seen that the decrease in activity of one order of magnitude is less pronounced than the decrease in coverage, which is more than three orders of magnitude.

The geometric current density referred to the active Pt surface results in the specific current density. Comparing the lower coverages of Pt submonolayers on Au(111) with a Pt(111), single-crystal enhancement factors of up to three orders of magnitude for the specific current densities were found. The catalytic activity thus strongly increases with decreasing coverage for both hydrogen reactions. Although the geometric current density absolutely decreases with decreasing coverage, as discussed above,

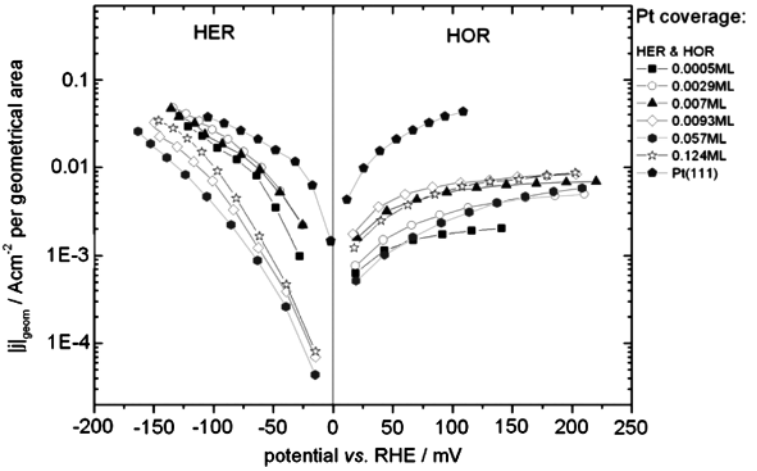

FIGURE 1.32 Tafel plot of HER and HOR with current density per geometric area for Pt submonolayers on Au(111) and Pt(111) in 1 M $HClO_4$ [141].

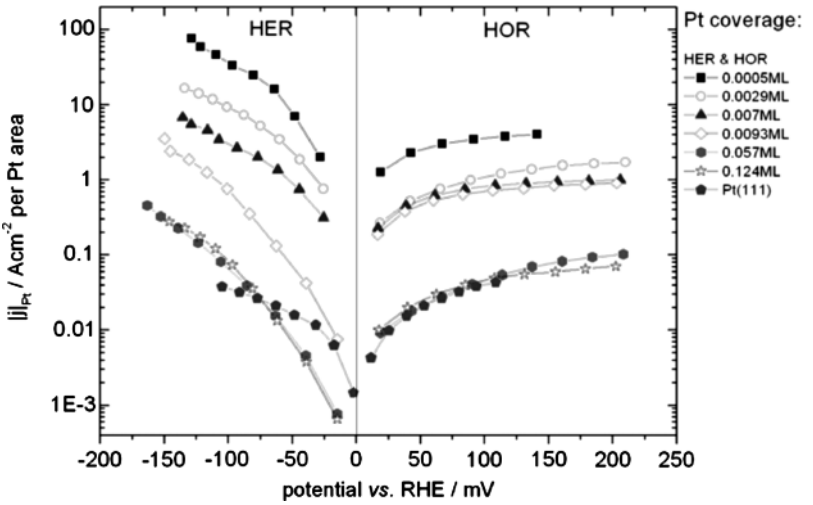

FIGURE 1.33 Tafel plot of HER and HOR with current density per Pt area for Pt submonolayers on Au(111) and Pt(111) in 1 M $HClO_4$.

the specific current density strongly increases. Because of very high currents, it seems that diffusion effects may play an important role in HOR. Comparing both branches in Figure 1.33, the HOR branch is lower at higher overpotentials compared to lower overpotentials, where HER and HOR are similar. This may lead to the assumption that an impact of diffusion limitation has to be considered although methods were used to avoid the diffusion effects. This is clearly shown in Figure 1.33, where the specific current density is plotted versus the overpotential for several Pt submonolayers on Au (111) and Pt(111). In summary, the specific activity for HER is about three orders of magnitude higher compared to Pt(111) and the specific activity of HOR is more than two orders of magnitude higher compared to Pt(111) (Fig. 1.33). Different explanations for the strong enhancement are given. As already mentioned in the Pd/Au(111) case, there is not one major parameter that causes this behavior. Also, for Pt deposited on Au(111), particle size effect, support effect, and high reactivity defects must be considered. Thus far it is unclear which effect plays the leading role or whether the enhancement is due to a combination of effects.

1.5.7 Summary

Adsorption and desorption processes were investigated on single-crystal surfaces by the Kolb's group [121,127,128]. Various indicators were found that underline the importance of Pd overlayer thickness and selection of support. Pd thickness as well as support influence the adsorption and desorption behavior as well as the electrocatalytic activity. The experimental finding were supported by theoretical work from the Nørskov group [129,130,148] and the Gross group [149,150] reported in Section 1.4. The experimental results for HER and HOR on monoatomically high Pd nanoislands deposited on Au(111) indicate a specific electrochemical activity that increases with

decreasing coverage [127,134,141]. A similar increase in specific activity was shown for the HER as well as for the HOR for Pt nanostructured Au(111) surfaces [141]. Although the net current densities for HOR are one order of magnitude lower than for HER, the enhancement of specific current density is nearly two orders of magnitude for both reactions. The lower concentration of reactants and thus a diffusion limitation in the case of HOR can affect this behavior. The enhancement was attributed to several effects. For decreasing Pd monolayers down to one monolayer, one has to consider a strain effect of the Pd overlayer according to the Nørskov model. The strong enhancement for the submonolayers was explained by a hydrogen spillover from the Pd particle onto the Au(111) support. Defect sites and steps do not have a big impact on electrocatalytic activity.

Similar results were also obtained by Kibler [127,135] for HER. In contrast to studies by the Stimming group [134,141], the other studies investigated the exchange current densities, and not the specific current densities, and an enhancement of a factor of ~ 4 was found comparing 1 ML with 0.07 ML Pd on Au(111). The importance of the free energy of hydrogen adsorption was underlined, whereas defect sites and steps often play an important role. An influence of the support was also provided with the background of theoretical calculations. Also, the Baltruschat group [144–146] performed several Pd-on-Au(111) experiments. It was suggested that the main part of the electrocatalytic activity is caused by the steps. Pd on the Au (111) terraces is not very active and thus has no influence on enhanced catalytic activity. A model based on a spillover concept from the hydrogen from Pd to the Au (111) support does not seem to be reasonable here, according to Hernandez and Baltruschat [144,145].

Markovic and Ross [142] studied the Pd-on-Pt(111) system. Here also, an improvement of the catalytic activity compared to pure Pt(111) was found. Decorating the Pt(111) surface with Pd enhances the performance toward HER and HOR. This effect can be clearly seen in Figure 1.28. A variation of the thickness was not done, but the positive effect of Pd was also demonstrated in this case.

Blocking the surfaces with different metal adlayers to show an inhibition effect was investigated by Markovic and Ross [142]. All three different metals, Cu, Pd, and Bi, decrease the electrocatalytic activity of Pt toward HOR. Thus, improving the activity with these model surfaces does not seem feasible. In this case, Pt is highly reactive and is inhibited by the metal adlayers.

1.5.8 Discussion

Pt/Au(111) [141] as well as the Pd/Au(111) systems [127,134,135,141] show a strong enhanced specific current density toward HER and HOR. Although the net current densities for the Pt on Au(111) are significantly higher than for the Pd on Au(111) system, both show similar behavior. An obvious enhancement of the specific electrocatalytic activity for Pt on Au(111) with decreasing Pt coverage with respect to HER and HOR is clearly seen in Figure 1.33. The specific current densities are approximately three orders of magnitude higher for small coverages of Pt on Au(111) as compared to Pt(111) surface for HER and more than two orders of magnitude higher

for HOR. A similar trend was found for the Pd on Au(111) system shown in Figures 1.26 and 1.27. The increase in specific reactivity is also more than two orders of magnitude, whereas the current densities of HOR are lower compared to the current densities of HER. According to the importance of Pt catalyst, the main focus in the discussion is on the Pt results but often refer to the well-investigated Pd/Au(111) system.

For a general understanding of HOR and HER activity of Pd- and Pt-modified Au(111) electrodes, several parameters have to be considered. One parameter is the influence of the substrate on the lattice constant of the Pd or Pt overlayer. According to the Nørskov model, a lateral strain on the metal overlayer causes a shift of the *d*-band center [130,134,137,139,151–154], resulting in a change in the electronic properties of the overlayer. For the Pd/Au(111) system the enhanced activity of Pd monolayers compared to Pd multilayers on Au(111) can be explained by a strain effect of the gold substrate on the Pd layer. Such strain effects gradually decrease with increasing thickness of the Pd layer [133]. This influence is confirmed by the reverse experiment with a support material with a smaller lattice constant. In case of tip-induced Pd particles on Cu(111), no enhancement for HER activity was found [155]. This is in line with expectation and theory, since copper has a smaller lattice constant than does palladium. Furthermore, Pt nanoislands electrodeposited on highly oriented pyrolytic graphite (HOPG) also show no enhanced activity for HER for mono- and submonolayers of Pt [156]. In this case, no influence of the support is expected, due to weak interaction between metal and support. Both results indicate that neither Cu nor HOPG as support enhance the electrocatalytic activity of deposited Pd or Pt particles. Therefore, strain induced by the support material seems to be an important parameter that enhances electrocatylytic activity for HER and HOR. This allows a better understanding of the increase in electrocatalytic activity of deposited Pd and Pt as a function of layer or particle thickness.

Nevertheless, it is important to consider that the most pronounced increase in HER activity was observed for submonolayers of Pt and Pd on Au(111). As is described in Section 1.6, Meier et al. [133] reported about nanoscale effects of single Pd particles that were deposited with an STM tip on Au(111) surfaces. The catalytic activity for HER is drastically depends on the height of the particles and increases by about two orders of magnitude going from particle height of 10 layers to particles of approximately two layers of height. Electronic effects induced by the substrate depending on the height of the deposited particle are also important. The argument of modified electronic properties due to a lattice strain of an isomorphic overlayer is applicable to Pt islands as well as to Pd islands, whether single particles or large nanostructured surfaces. Since the lattice mismatch between gold (0.408 nm) and platinum (0.392 nm) is 4%, and between 4.8% gold and palladium (0.389 nm), it is logical to expect a similar increase in activity based on the Nørskov effect for the Pt/Au(111) as well as for the Pd/Au(111) system. For a further understanding, it has to be considered that tip-induced Pd islands on Au(111) were varied in height. The electrochemically deposited monoatomic Pd islands on Au(111) were varied in coverage; nevertheless, in both cases an enhanced activity is observed. The increasing activity for submonolayers of monoatomically high Pd and Pt with decreasing

amounts of deposited metal may be ascribed not only to a lattice mismatch but also to an additional effect. According to the Nørskov model alone, the specific activity of nanoislands of various coverages should be identical.

The spillover model, introduced by Eikerling et al. [147], was described in more detail in Section 1.3. Enhanced catalytic activity of Pd nanoislands is attributed to spillover of atomic hydrogen from the Pd sites to the gold surface. A kinetic model was developed for observed increased activity of single particles on Au(111) surfaces. A spillover of atomic hydrogen from Pd islands with a high coverage of hydrogen to near-hydrogen-free gold surface can energetically be a downhill process [133]. The charge transfer takes place at the Pd islands and the recombination occurring on the Au(111) seems reliable. A potential application of this model to the reverse hydrogen oxidation reaction involving both surface catalyst as well as Au(111) can also be imagined, although it remains difficult to prove this in detail. Thus, the increase of catalytic activity for monoatomic submonolayers of Pd and Pt on Au(111) compared to monolayers could be understood by the involvement of the Au(111) surface as an additional storage of adsorbed atomic hydrogen.

An alternative explanation for the observed increased electrocatalytic reactivity of submonolayers could be based on a possibly higher activity of low coordinated surface atoms such as step sites as proposed by Hernandez and Baltruschat [144,145]. It was found that a Pd monolayer is more reactive than Pd multilayers, which is in good agreement with a strain effect induced by the Au surface. The exchange current density of submonolayers of Pd down to 0.2 ML is independent of Pd coverage. Furthermore, it was demonstrated that codeposition of copper at Pd submonolayers results in an inhibited HER activity. It is suggested that the Pd at the steps controls the kinetics of hydrogen evolution on stepped gold surfaces modified by Pd. In case of Pd nanoislands on Au(111), the reactivity of HER is significantly larger, by a factor of $\sim$5, such as at an overpotential of 50 mV. Analysis of nanostructured Au(111) electrode surfaces reported by Pandelov and Stimming [134] shows no correlation of current density for HER with the number of Pd edge versus Pd terrace atoms on Au(111). The same result was found by Meier et al. [133] from an analysis of single Pd particles on Au (111). Hence, the number of low coordinated atoms such as edge atoms does not seem to be the dominant factor controlling HOR and HER activity on nanostructured Au(111) surfaces. From the experimental results reported, it remains difficult to develop a complete model for HER and HOR on nanostructured Pd/Au(111) and Pt/Au(111) surfaces in spite of the strong effects observed.

Nevertheless, all experimental findings for the extended Pt and Pd nanostructured surfaces presented here tend to show improved catalytic behavior. Although the authors prefer different explanations for their findings, it is not possible at the moment to neglect one of the approaches. Briefly summarized, the kinetics of HER and HOR are obviously influenced by several parameters, and it remains important to understand the origin of these differences. Although Pt is among the best catalysts for hydrogen related reactions, there is still potential for improvement. On the basis of the reported experimental results, it can be stated that the positive effect of Pd and Pt lattice expansion on Au(111) for hydrogen-related reactions is one of the fundamental issues remaining to be understood in more detail.

1.6 INVESTIGATIONS OF HYDROGEN-RELATED REACTIONS ON SINGLE Pd PARTICLES

1.6.1 Introduction

Planar surfaces have been thoroughly investigated, and most of the reactivity measurements are referred to these extended electrodes [157–163]. In contrast to, nanostructures and nanoparticles often behave differently than bulk material. Therefore novel techniques were developed and applied to investigate the changed properties in the nanometer scale. One possible approach is the scanning electrochemical microscope (SECM), which uses ultramicroelectrodes (UMEs) for investigation. With this technique a resolution of about 100 nm is achievable, which is limited by the geometry of the UME. Meier et al. [164] introduced a technique that uses a tip of an electrochemical scanning tunneling microscope (EC-STM) as probing sensor. Because of the tunneling effect and thus the high precision, atomic resolution is possible, which is several orders of magnitude in geometric precision lower than in other techniques. In this way, the electrocatalytic activity of single Pd particles on Au(111) support toward hydrogen evolution was investigated in situ [164,165]. In this approach the hydrogen evolution at the Pd particle was indirectly measured via the detection of the oxidation of the evolved hydrogen at the tip. Therefore the STM tip was used as a local sensor measuring the activity of a single Pd particle. This approach allows a complete in situ investigation of single particles from characterization to reactivity measurements. In Section 1.6.2 the STM tip is reviewed as a tool for local nanostructuring. The principles of local investigations with the STM tip with their possibilities and limitations are shown in Section 1.6.3. Experimental as well as theoretical principles of particle preparation and stability will follow. Section reviews the results obtained from single Pd particle experiments supported on Au(111). These results are discussed and compared to those for large nanostructured electrodes.

1.6.2 STM Tip as a Tool for Local Nanostructuring

Local methods for nanostructuring enable modifications of the substrate on a defined position by a direct impact. This approach to creating nanostructures using macroscopic techniques is called a *top–down approach*, which enables the creation of defects or deposition of clusters on the surface. All these techniques are direct methods, so the structures are directly fabricated in contrast to a mask for indirect deposition. Typical techniques for nanolithography are photolithography, X-ray lithography, electron- and ion-beam lithography, or the scanning probe microscopy techniques such as STM and atomic force microscopy (AFM).

Here different techniques for nanolithography are discussed in detail using STM and EC-STM. In the electrochemical environment there are many different options for using the STM tip to create a cluster or induce a defect. The first attempt uses the tip and forces a contact with the substrate (see Fig. 1.34a). In this way, a defect is created for metal deposition in a second step. A gentle approach is shown in Figure 1.34b that is quite substrate-sensitive. The tip removes only a tarnishing film from the substrate and

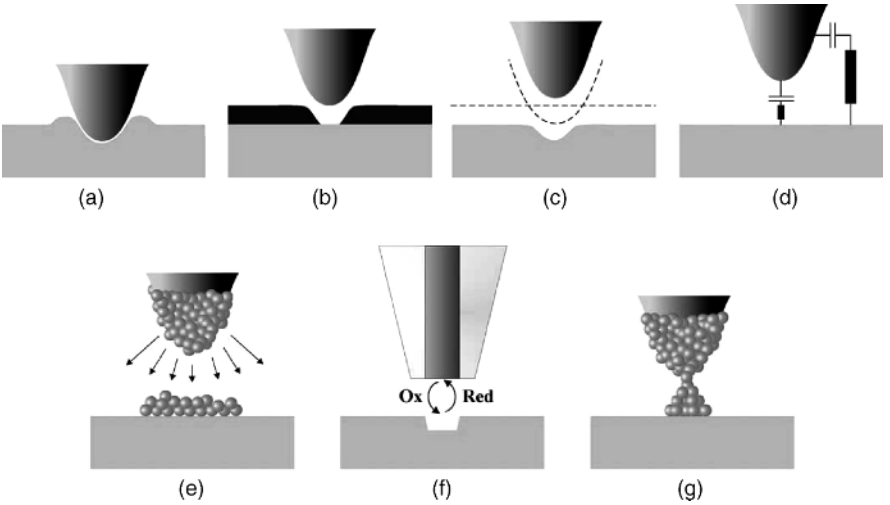

FIGURE 1.34 Different methods for nanostructuring with an STM tip: (a) mechanical impact; (b) removal of a tarnishing film; (c) double-layer crosstalk; (d) pulsed double-layer charging; (e) burstlike dissolution from the tip; (f) SECM with a nanode; (g) jump-to-contact method [181].

allows metal deposition. Studies at the system Cu on Au with sodium dodecylsulfate films have been reported [166]. The double-layer crosstalk in Figure 1.34c has to be included if the electrochemical double layer of the tip and the substrate interferes. A loss of the potential control of the substrate beneath the tip can result. Different groups investigated the Cu/Cu^{2+} [167] and the Ag/Ag^{+} [168] systems, where dissolution of bulk metal was induced by a very close approach of the tip. The Ertl group [169,170] used the so-called electrochemical machining technique to create structures. An ultrashort pulse was applied between tip and substrate in nanosecond regime for etching processes. Due to the time dependence of the double layer, charging on the upper or lower part this technique is used to set the pulse in such a way that only the tip apex interacts with the substrate potential (Fig. 1.34d). Therefore, it is possible to dissolve metal by oxidizing it in a small area. A quite easy way for tip-induced nanostructures is the burstlike method depicted in Figure 1.34e). The metal on the tip is deposited directly under the tip [171,172]. Schindler et al. [173] explain the effect with a high metal ion concentration after the deposition process that shifts the Nernst potential for the surface under the tip. Figure 1.34f) shows the scanning electrochemical microscopy (SECM). Next to the previously mentioned techniques, SECM can be used for detection of electrochemical processes on a micrometer scale. Especially in the field of electrocatalysis, SECM is a powerful tool for direct investigations of particles. More details will be found in the literature [174,175]. Most previous studies reported in the literature deal with deposition of clusters on substrates induced by the "jump to contact" method (Fig. 1.34g). The tip gets in contact with the substrate without destroying it. This effects a formation of a metal bridge, the so-called connective neck, which will break if the tip is retracted. Different

groups use this technique to create large arrays from different metals on different substrates [176–180]. In Section 1.6.3 methods using massive metal tips loaded with another metal from a solution are discussed. The tips consist of platinum with electrodeposited palladium for preparing single Pd nanoparticles, whereas the jump-to-contact method is used.

1.6.3 Principles of Single Pd Particle Preparation—Computer Simulation and Experiments

Scanning tunneling microscope tips have been used in many different approaches to generate nanoparticles on well-defined supports [164,165,173,176, 181–188]. Creation of large nanostructured electrodes with particles, single-particle reactivity measurements, and investigation of magnetic properties are several examples of single-nanoparticle investigations using STM. Different methods of using the STM tip for nanostructuring are discussed elsewhere [181] and are reviewed above. In one method reported in the literature [164,165,173,176,183] the tip is loaded with metal by electrochemical deposition from the electrolyte. A tip created by this technique is schematically shown in Figure 1.35a, where the bright atoms are tip atoms and the dark ones are the deposited metal. The tip is moved to the support and brought into contact (Fig. 1.35b). The jump to contact occurs and a connective neck is built (Fig. 1.35c). The tip is subsequently withdrawn and some atoms from the deposited metal on the tip will remain on the surface and yield a nanoparticle (Fig. 1.35d). The particle size is dependent on the distance to the tip, and hence the penetration depth into the surface and, of course, the geometry of the tip. It was shown that with larger movement of the tip in the z direction after building a connective neck, the particle size and hence the number of atoms per particle will increase. Interestingly, with increasing particle size the number of Au atoms also increases and a stable alloy is formed whereas the Au atoms are detached from the surface. Smaller particles generally consist only of Pd atoms.

The abovementioned increase in Au atoms stabilizes the particles as a result of the stable Pd–Au alloys and inhibits the dissolution compared to small particles. This assumption was also theoretically investigated using Monte Carlo simulation. The electrochemical potential μ of the particles was fixed and the number of atoms was varied. A series of simulations were performed on the basis of computational calculations, which are shown in Figure 1.36. The size and the composition of the particles are plotted versus the distance of the tip after experiencing a jump to contact. Calculations were performed for different electrochemical potentials of Pd. The initial configuration corresponded to the end configuration of the atom dynamic simulation; hence the cluster evolution was followed and the dissolution or growth of the cluster could be determined. It was shown that the particles grow at electrochemical potentials higher than -3.8 eV and completely dissolve at smaller values. The value of -3.8 eV is smaller than the cohesive energy of Pd of -3.9 eV, and thus it is suggested that particles are less stable compared to bulk Pd. Dissolution of particles fits well to the experimental results, which showed that dissolution starts at the base and is fast for small particles with a few atoms.

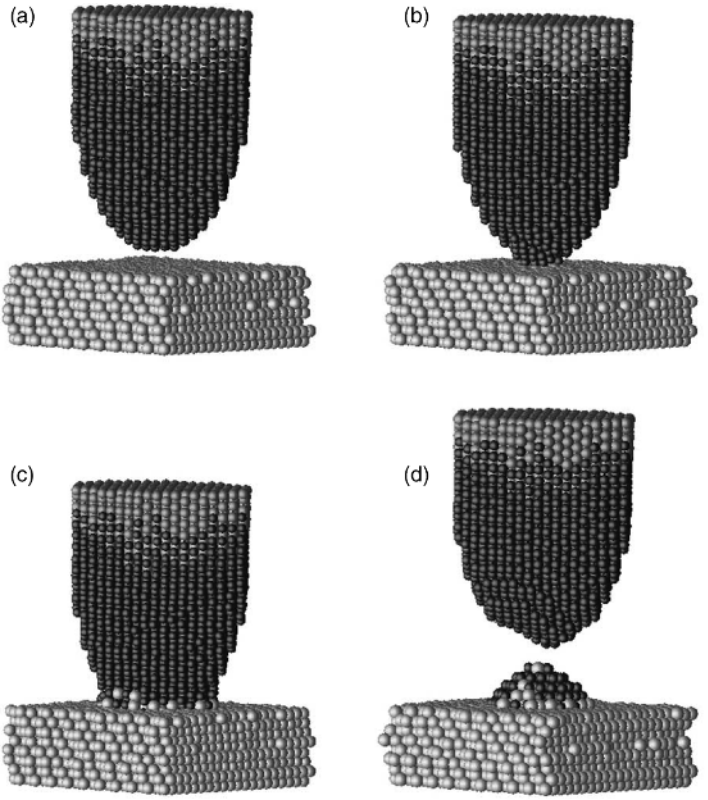

FIGURE 1.35 Snapshots taken during the generation of a Pd cluster on Au(111): (a) initial state of the system, $\Delta z = +/2.04$ Å; (b) jump to contact, $\Delta z = /0.0$ Å; (c) closest approach, $\Delta z = -6.37$ Å; (d) final state, $\Delta z = 11.04$ Å [177].

Particles with different heights and diameters were also experimentally generated and examined (Fig. 1.37). The differences in geometry are influenced by the folding of the shape of the tip and the shape of the particle. It was found that higher particles also have larger diameters. For a precise evaluation, particle height is plotted versus the approach of the tip toward the surface. At a certain point, cluster height increases with increasing values of Δz. The jump to contact occurs between -0.5 and -0.6 nm. Below that the tip is not in contact with the surface, and hence no particle is created. These experimental results agree very well with theoretical ones from Figure 1.36. Although the numbers of atoms shown in Figure 1.36 have been calculated, it is necessary to build a jump to contact to create particles, and it is also obvious that with deeper z-direction of the tip, movement particle height increases.

Experimentally generated single Pd particles on Au(111) are shown in Figure 1.38. All particles were produced in situ and characterized using electrochemical scanning tunneling microscopy. As can be seen, the particles differ in diameter and height, which vary with movement of the z-direction piezo during particle generation

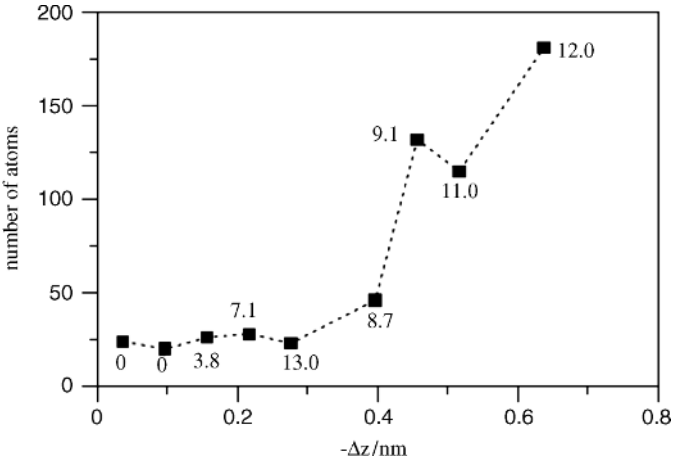

FIGURE 1.36 Number of atoms in the clusters obtained by computer simulations. The distance of closest approach is referred to as "jump to contact." The numbers close to the points give the percentage of gold atoms in the cluster [177].

and tip geometry. It was shown that the particles are stable for several hours but in some cases they their morphology changes and increasing particle diameter causes an increase in particle height, which is in agreement with the theoretical findings. A detailed description of particle stability and change in morphology follows. The particles are placed on large Au(111) terraces, guaranteeing no influence of defects of the support.

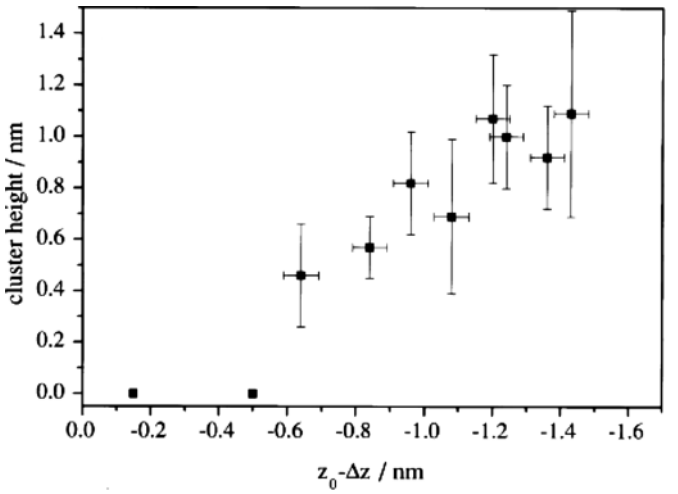

FIGURE 1.37 Height of Pd clusters on Au(111) as a function of distance of closest approach during generation [177].

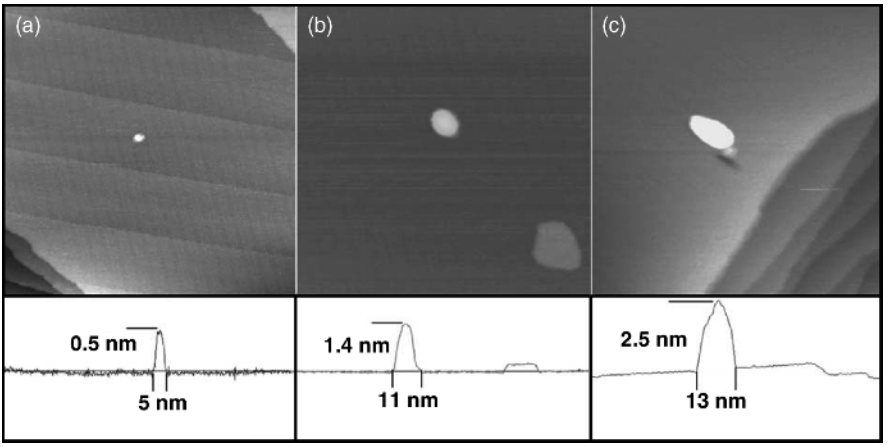

FIGURE 1.38 In situ STM image of tip-induced palladium particles: (a) one particle of 0.5 nm height; (b) particle of 1.4 nm height; (c) one larger particle of 2.5 nm height. All images are $100 \times 100\,\text{nm}^2$. All particles on Au(111) in 0.1 M H_2SO_4. $I_{\text{tunnel}} = 1$ nA, $U_{\text{WE}} = 400$ mV, $U_{\text{tip}} = 500$ mV [165].

Experimental and theoretical findings provide a consistent picture of particle generation using electrochemical STM. Increasing movement of the STM tip in the z direction induces increased particle size and particle stability. It was suggested that the stability of large particles is achieved mainly by Au atoms from the support forming stable alloys. In contrast, small particles contain only Pd atoms and thus are easily dissolvable.

1.6.4 STM Tip as Local Sensor Investigation of HER

Investigating single nanostructures such as particles of a few nanometers in diameter requires special techniques. Under electrochemical conditions it was demonstrated by Meier et al. [164] that an STM tip can be used as local sensor. With this technique it was possible to investigate single Pd particles supported on Au(111) toward HER. The purely in situ method combines generation of the Pd particles with the tip, characterization of the deposited particles, and subsequent measurement of the particle reactivity. Here, the hydrogen evolution was chosen for investigation because of its importance in electrochemistry. The catalytically active particle on the inert Au(111) support was directly observed with the STM tip. With electrochemical potential control of the support and the tip, it was possible to independently apply appropriate potentials. Therefore, it was feasible to evolve hydrogen on the Pd particle, whereas the tip was at a potential inducing the adjacent oxidation of the evolved hydrogen. The tip was placed ~ 10 nm above the Pd particle and thus collected most of the evolved hydrogen. With the very high sensitivity of the preamplifier in the STM setup, which is normally used to control the tunneling current feedback, it is possible to resolve currents down to several picoamperes. This method is suitable for single particles

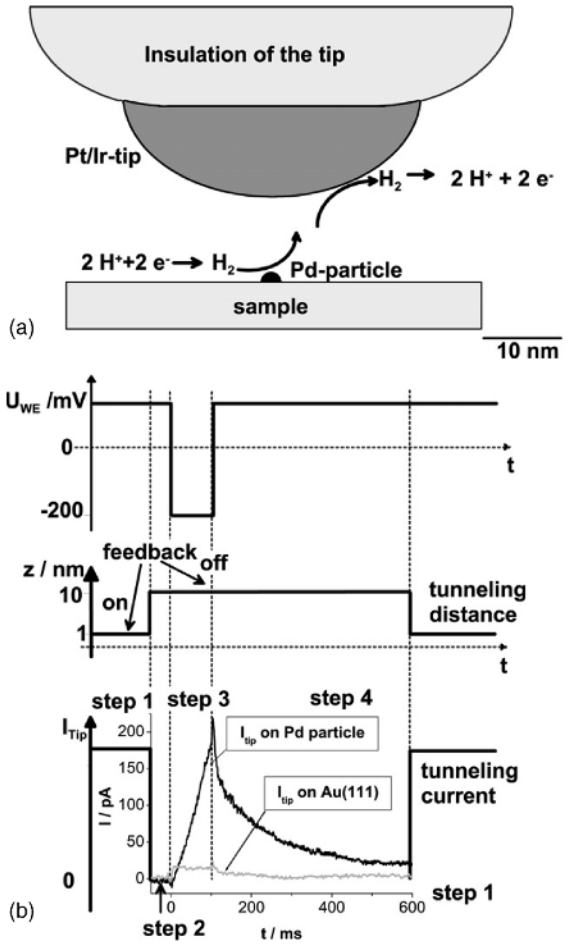

FIGURE 1.39 (a) Illustration of the proton reduction reactivity measurement; (b) principle of the method: (1) the structure of the palladium particle is characterized; (2) the tip is positioned over the cluster and retracted while the feedback control is switched off; (3) a potential pulse of 100 ms duration is applied to the sample while the tip potential is kept constant and the hydrogen oxidation current on the STM tip is recorded; finally, the feedback control is switched on and the STM tip is back in tunneling mode [164].

and very small coverages. Using higher coverages leads to interferences due to the collection of evolved hydrogen from several particles. The high precision in vertical as well as horizontal resolution due to the nature of the STM using the tunneling effect allows a highly defined positioning measurement system. A detailed description of the local measurement technique with the STM tip is shown in Figure 1.39a, which includes the reaction pathway of HER at the Pd particles and the subsequent oxidation of the evolved hydrogen at the tip. Figure 1.39b is a detailed recording of the applied voltage on the working electrode, the distance of the tip from the support, and the

current transient measured at the tip. In the following text all steps are described in detail. The tip was used to create and characterize the Pd particle on the support as a first step. After the scan stopped, the feedback of the STM was turned off and the tip was retracted (step 1). The potentials of the working electrode and the tip were still positive and tunneling current dropped to ~ 0 pA (step 2). Applying a potential negative of the hydrogen equilibrium potential induced the production of hydrogen from protons in the electrolyte. Protons diffused through the electrolyte to the tip and were oxidized (step 3). The current at the tip is the oxidation current of the evolved hydrogen at the Pd particle. In the last step (step 4) the current was recorded, and decreased because there was no further hydrogen evolution at the particle. This technique allows circumvention of transport limitations, which is not easily achievable for flat surfaces. Assuming a semihemispherical particle and thus hemispherical diffusion, one can estimate the diffusion-limiting current at $\sim 10^5$ A/cm^2 for a particle with 2 nm radius. Therefore, it can be expected that diffusion limitation is not achieved with a large range of overpotentials.

1.6.5 Stability of Pd Nanoclusters on Au(111)—Experimental Results

Palladium nanoparticles were deposited with STM as described before. A contact between the tip and the support builds a connective neck and thus withdrawing the tip yields a particle. Some atoms of the tip stay at the surface and build a particle. For investigation, the particles must be stable on the support. The requirements for performing HER reactivity measurements on deposited Pd particles do not stipulate that no Pd^{2+} ions be in the solution. Especially in this case, potentials are required that are far more negative than the Pd equilibrium potential in a Pd^{2+}-free solution. Thus the Pd particles are in a metastable state from a thermodynamic perspective. To gain further insight into the stability of Pd nanoparticles, the dissolution was investigated. Four different particles were regarded and are shown in Figure 1.40a. Particles A, B, and C have the same height but differ in diameter; particle D is larger in height and diameter. Figure 1.40b shows the change in particle height over time at a potential of 330 mV versus RHE. This potential is positive enough to slowly dissolute the Pd particles in the Pd^{2+}-free electrolyte. Obviously the change in particle height is not continuous. The decrease in particle height is stepwise with 0.26 nm per step. This value could not be allocated to any lattice constant of Pd or Au. As already seen in theory, the small particles decay faster compared to the big particle, which is still not completely dissolved. It was suggested that the particles consist of a layer structure. Dissolution of particles starts from steps and not from the top, which indicates that the low coordinated atoms are dissolved first. Furthermore, after dissolution of the larger particles, holes in the support were found next to the particles, indicating alloying of the Pd particles with the Au support. It was also concluded that smaller particles mainly containing Pd are less stable compared to larger ones consisting of more Au atoms and forming stable alloys. In summary, the experimental results presented are in line with the theoretical ones described before. Larger particles are more stable than smaller particles as a result of alloying, and small clusters practically consisting of Pd are completely removable from the support.

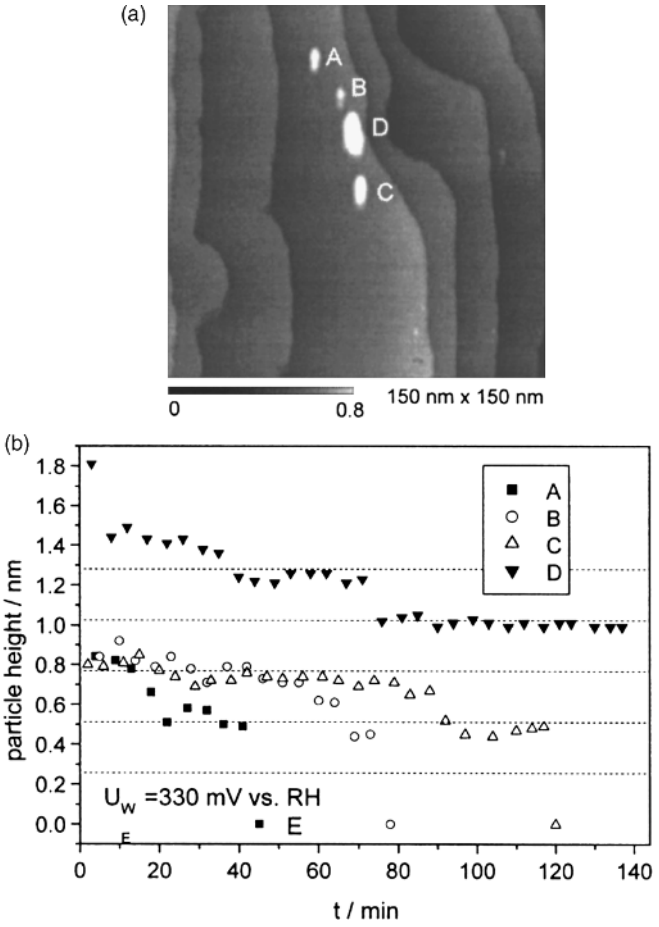

FIGURE 1.40 (a) STM image of Pd clusters on Au(111) in 0.1 M H_2SO_4 immediately after generation, with $I_{tip} = 1.1$ nA, $U_{bias} = 170$ mV; (b) change in particle height with time at 330 mV versus RHE.

1.6.6 Reactivity Measurements of Pd Single Particles on Au(111)

Investigating nanoparticles usually means that a large number of particles are considered and the overall behavior is observed. Lowering the number of particles requires a high current resolution setup and sufficient signal-to-background ratio, which is not easily achievable. Also, agglomeration, size distributions, inhomogenities, and diffusion limitations of reaction partners have to be considered. Therefore, a technique investigating only one particle was introduced by Meier et al. [164,165]. As explained in a previous subsection, the tip was used to measure the reaction products. In this case the evolved hydrogen was oxidized at the tip and hence an indirect reactivity was measured. The catalytic activity was shown to be

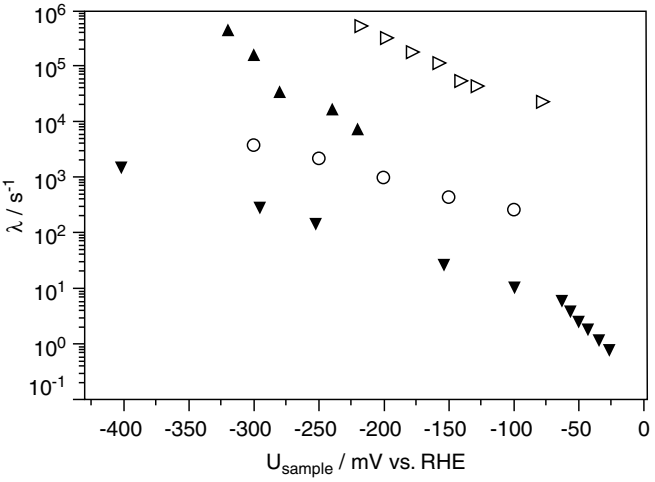

FIGURE 1.41 Tafel plots of three different Pd particles on Au(111) in 0.1 M H_2SO_4: ○, Pd particle with 10 nm height and 200 nm diameter; ▲, Pd particle with 2.5 nm height and 12 nm diameter; ▷, three Pd particles with 0.5 nm height and 6 nm diameter; ▼, polycrystalline Pd [192].

strongly dependent on particle size, especially particle height. Therefore, particles of different height and diameter were investigated. For different overpotentials applied at the single Pd particle, the Au(111) support hydrogen was evolved and the activity was measured. Figure 1.41 shows a Tafel plot for different Pd particles deposited on Au(111). It is obvious that with decreasing particle height, increasing activity is observed. The increase in activity is at least two orders of magnitude, comparing 200 nm with 6 nm in diameter. Detailed study revealed that the current densities, especially for particles with a height of 0.5 nm, are highly reactive, up to two orders of higher magnitude compared to the flat Pd surface. A change in the Tafel slope was also indicated and was explained by surface diffusion effects on the support [189]. The changed Tafel slope also indicates that the reaction mechanism of the HER is different. Whereas a Tafel slope of 118 mV suggests a rate-determining step of the discharge of the protons, a Tafel slope of 29 mV theoretically predicts the recombination of two adsorbed hydrogen atoms as the rate-determining step. Because of the mixed Tafel slope values, it was suggested that recombination becomes more important since the discharge of protons should be rapid. The enhanced activity was discussed regarding several approaches. An influence of low coordinated atoms on reactivity was not found. Charging of the particles due to different workfunctions and a modified double layer were also excluded. Applying the model of the changed *d*-band center [190,191] was suggested to explain the enhancement.

An important relationship was found by correlating the activity with particle height (see Fig. 1.42). A strong increase in activity was observed with decreasing particle height. An influence of the number of low-coordination atoms was excluded.

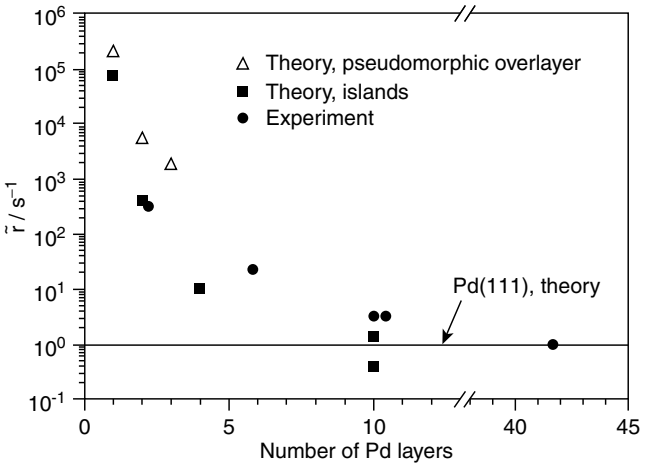

FIGURE 1.42 Semilogarithmic plot of the relative reaction rate r versus particle height. Full circles represent experimental data ($U_{WE} = 200\,mV$); open triangles, theoretical predictions for pseudomorphic overlayers, obtained from DFT calculations; full squares, theoretical predictions for islands, obtained by combining the DFT calculations with molecular dynamics [165].

STM images were evaluated and the ratio of low-coordination atoms to surface atoms was determined. Study of two different effects was suggested: (1) the surface structure of the Pd particle and (2) the hydrogen bonding to the Pd layers. It was shown [193] that Pd grows in (111) orientation on Au(111). Because of the different lattice constants, the Pd overlayers are strained by $\sim 4.8\%$. Up to now it has not really been clear which function should be applied for mismatch versus layer thickness. Molecular dynamics (MD) calculations showed that single-layer islands are pseudomorphic while two Pd monolayers introduce misfit dislocations. It was also shown that for even four monolayers a strain can be observed in the Pd overlayers. Also, the adsorption energy of hydrogen to Pd overlayers in Au(111) was calculated using DFT, whereas the adsorption energy is closely related to the reactivity [165]. In Figure 1.42 shows that the theoretical calculations for islands that are one to three monolayers high are more reactive compared to the Pd(111) bulk. A strong enhancement is observed by increasing the height of islands as well as pseudomorphic overlayers. Experimental findings and the theoretical calculations showed the same trend seen in Figure 1.42. The enhancement in reactivity is caused by a strain of the Pd overlayers induced by the Au support with a larger lattice constant. Therefore, the electronic properties and thus the binding energy to hydrogen are changed.

Similar results were also found on extended Pd nanostructured Au(111) surfaces by Pandelov and Stimming [161], which supports the single-particle approach. Nevertheless, with the advantages of only slight diffusion limitation and the possibility of investigating single particles under electrochemical conditions, this method and the results are unique.

1.6.7 Summary

A combination of theoretical and experimental results was reviewed regarding generation, stability, and activity of single Pd nanoparticles on Au(111). It was shown that generation of single particles is dependent on the movement of the STM tip in the z direction and the geometry of the tip. With increasing movement toward the surfaces, increasing particles sizes were experimentally obtained and theoretically calculated. Larger particles form Pd–Au alloys with Au atoms from the support, which stabilize the particle and inhibit the dissolution, whereas smaller particles consist only of Pd and are completely dissolvable. The electrochemical STM tip as a probing sensor was used to investigate the HER on single Pd particles in Au. It was found that with decreasing particle height the reactivity strongly increases. This finding is in line with the Nørskov model, which explains the enhanced reactivity due to a shift in the d-band center and thus in changed adsorption energy to hydrogen. Similar results were also reported for large Pd nanostructured Au(111) surfaces from Pandelov and Stimming [161]. For this reason two different experimental approaches show the same trend: namely, that with decreasing particle height rather than coverage, the activity toward HER is increased. The method of investigating single particles is a powerful tool for direct investigation of the catalytic activity in the nanometer scale without the limitations due to extended surfaces. Although the experimental approach is sophisticated and time-consuming, new insights into reactivity behavior influenced by the support were found. Together with findings from extended surfaces, an additional argument shows the importance of the support and the influence on reactivity.

1.7 STUDIES OF HYDROGEN-RELATED REACTIONS ON CARBON-BASED SYSTEMS

1.7.1 Introduction

In this last section of the chapter we present an overview of studies performed on carbon-based systems, for hydrogen-related reactions. Carbon has been the material of choice for many years because of its high electrical conductivity, low cost, and high availability. Carbon is a conventional support used in the present technology of fuel cells. There are many papers, some of which are presented here, devoted to studying HER and HOR mechanisms using metallic nanoparticles on carbon-based supports. Another topic of interest is the activity of these catalysts for CO oxidation in combination with their activity toward HER and HOR.

Carbon monoxide poisoning is a major issue in today's fuel cell technology since it impedes fuel cell commercialization. Fuel cells operating with industrial hydrogen, hydrogen feedstreams derived from carbon-based fuels or alcohols, present deactivation issues of the anode catalyst even with small traces of CO. Therefore, although Pt is shown to be a very good catalyst for HER and HOR, it is deactivated strongly by CO, leading to high overpotentials. Hence, a catalyst is needed that combines the ability to oxidize both CO and H_2 effectively.

1.7.2 HOR and HER Studies on Carbon-Supported Metallic Nanoparticles

Gasteiger et al. [194] studied H_2 and CO electrooxidation on Pt, Ru, and Pt–Ru catalysts using the rotating-disk electrode (RDE) method. Binary platinum catalysts consisting of alloy mixtures of Pt with other metals such as Ru, Rh, and Sn showed enhanced activity toward CO oxidation. These mixtures facilitate the oxidation of CO by providing oxygen-containing species, therefore increasing the active sites for hydrogen oxidation. Pt–Ru alloys are commonly used nowadays as supported catalysts for direct alcohol fuel cells. Gasteiger et al. [194] studied the alloying effect on H_2 and CO oxidation using simple but effective sample geometry. They used arc melting to prepare pure Pt, pure Ru, and Pt : Ru (1 : 1 atomic ratio) alloy samples with a small diameter (∼6 mm). As seen in Figure 1.43, the sample containing Pt–Ru alloy showed enhanced activity toward CO oxidation compared to pure Pt sample. They also observed that the alloy sample showed identical activity compared to pure Pt sample toward H_2 oxidation, as shown in Figure 1.44. Although the pure Ru sample exhibited the optimum behavior toward CO oxidation, its activity toward H_2 oxidation was many orders of magnitude lower.

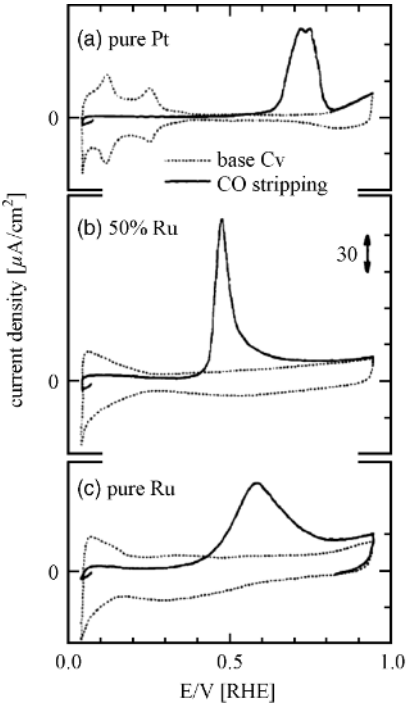

FIGURE 1.43 CO stripping voltammetry of sputter-cleaned electrodes in 0.5 M H_2SO_4 on (a) Pt, (b) Pt–Ru, and (c) Ru. Straight line indicates first positive-going sweep; dashed line, negative-going sweep after stripping of CO, followed by a positive-going sweep. Scan rate was 20 mV/s [194].

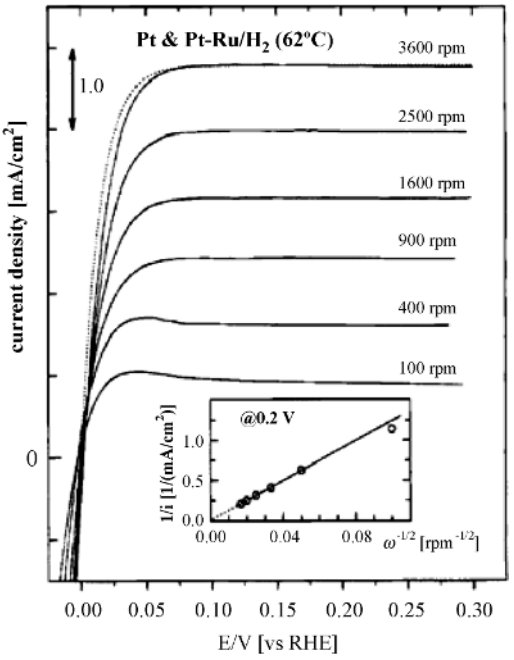

FIGURE 1.44 Hydrogen reduction and oxidation current densities during positive-going sweeps (20 mV/s) on Pt and Pt–Ru electrodes saturated with H_2 at 62 °C [194].

Sasaki et al. [195] investigated bimetallic catalysts consisting of Pt submonolayers deposited on Ru and Au nanoparticles supported on carbon. The catalysts were investigated for hydrogen oxidation as well as oxygen reduction. Deposition of Pt on Ru was carried out by immersing the Ru catalyst on a solution containing Pt, while Pt deposition on Au was achieved by redox displacement of a Cu underpotential deposited monolayer. Two types of samples were prepared and included Pt/Ru and Pt/Au planar surfaces as well as carbon supported catalysts. Representative TEM pictures of the supported PtRu catalysts are shown in Figure 1.45.

The Pt–Ru catalyst showed enhanced activity for hydrogen oxidation in RDE configuration compared to commercial catalysts where CO-contaminated H_2 was used as a fuel (Fig. 1.46). The results showed that mass specific activity for H_2 oxidation of $PtRu_{20}$ catalyst is 3–4 times larger than for commercial catalysts. Also, CO tolerance tests proved the $PtRu_{20}$ catalysts to be superior to commercial ones.

Chen and Kucernak [196] investigated the kinetics of hydrogen oxidation reaction on single-Pt-particle-supported carbon. The advantage of their method is that they could quantify the mass diffusion properties. They also studied the role of the H_{upd} in the electrochemical oxidation of hydrogen molecules. As discussed previously, HOR involves atomic hydrogen as adsorbed species. The role of adsorbed hydrogen in HOR is not yet fully understood. It is believed that it either could be the intermediate involved in oxidation of dihydrogen or acts as blocking intermediate, hindering the reaction. Their sample preparation included

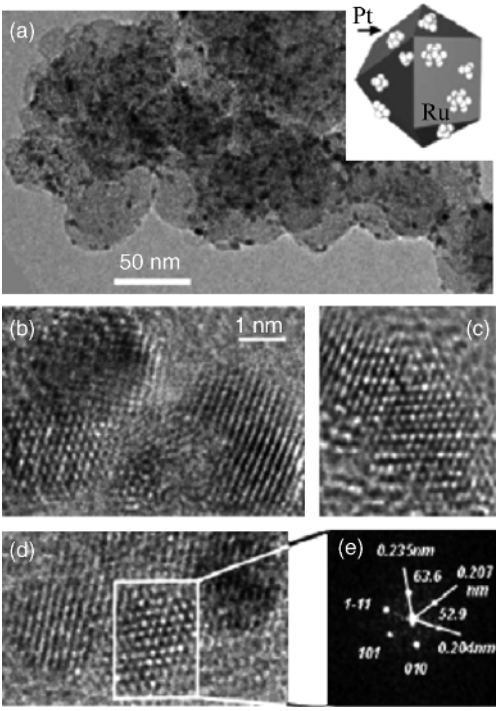

FIGURE 1.45 TEM micrographs of the $PtRu_{20}$ catalyst prepared by spontaneous deposition of Pt on Ru nanoparticles: (a) low magnification morphology of the metal particles (black dots indicate average size ~2.5 nm) on carbon spheres (average size ~50 nm); (b–d) high-resolution images showing atomic resolved lattice structures; (e) diffractogram obtained from the high-resolution image shown in (d) with measured the angles and lattice spacings that are consistent with hexagonal close-packed (hcp) Ru single-crystal structure [195].

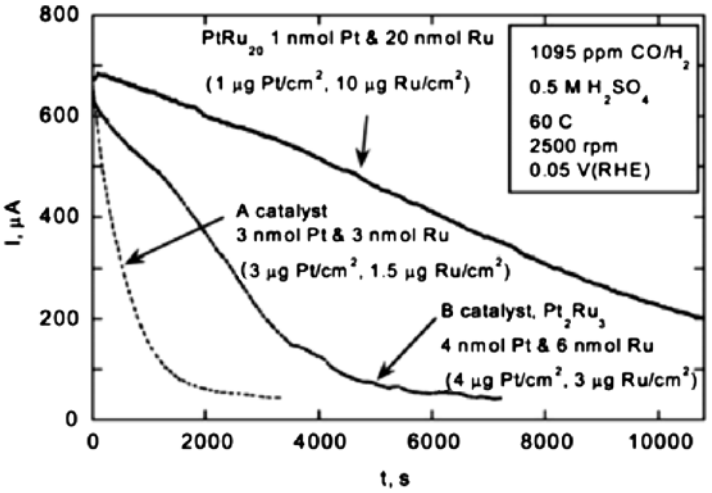

FIGURE 1.46 Comparison of the CO tolerance of three catalysts based on the current as a function of time for the oxidation of H_2 with 1095 ppm of CO at 60°C for the $PtRu_{20}$ and two commercial electrocatalysts at 0.05 V with the loadings indicated in the graph. A considerably larger CO tolerance is seen for the $PtRu_{20}$ catalyst [195].

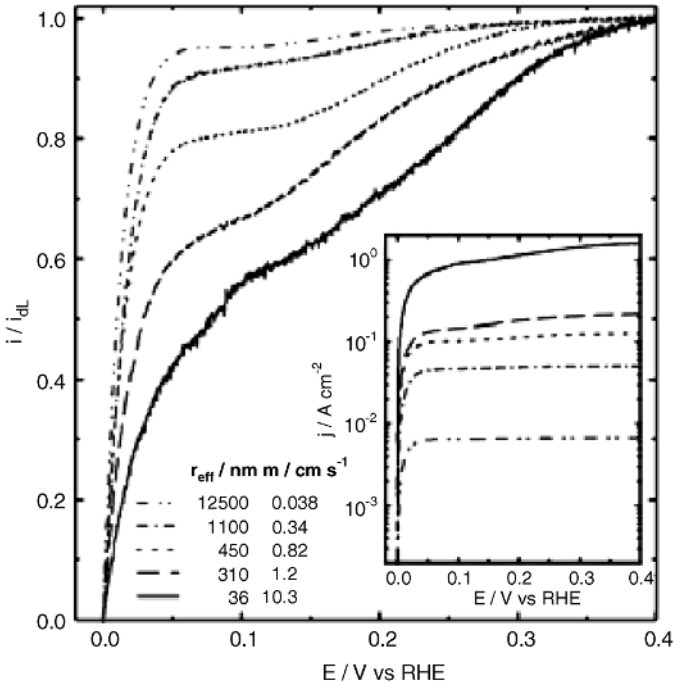

FIGURE 1.47 Current–potential curves obtained on particle electrodes accompanying the oxidation of hydrogen in 0.1 mol/dm^3 H_2SO_4 solution saturated with CO free hydrogen gas. The currents are normalized by the limiting values read at about 0.45 V. The numbers in the figure indicate the particle radius and give the mass transport rate for that particle assuming hydrogen diffusion coefficient of 3.7×10^{-5} cm/s. Scan rate is 5 mV/s. The inset shows the current density–potential plot for each of these particles [196].

electrochemical etching of carbon fibers, followed by insulation of the latter leaving a very small area exposed (down to a few nanometers). Single Pt particles are then deposited by electrochemical deposition. The results of the study toward HOR are shown in Figure 1.47.

As is shown, the current densities vary almost three orders of magnitude for the range of particles examined. Also, the features of the curves are different from those obtained from RDE experiments. For small particle radii there are two limiting current plateaus indicating two separating processes involved in HOR. As the particle radius increases, the two different limiting currents diminish. The authors explain this behavior to be a result of decreasing the ratio between reaction rate constant and mass transport coefficient. A model is also presented showing that the first plateau is due to the limiting rate of the Tafel reaction. Additionally, they conclude that H_{upd} is a reaction intermediate rather than an inhibitor of HOR.

Arenz et al. [197] examined the catalytic activity of various carbon-supported Pt–Sn catalysts toward oxidation of H_2, CO, and H_2/CO mixtures. Typical micrographs of the catalysts studied are shown in Figure 1.48.

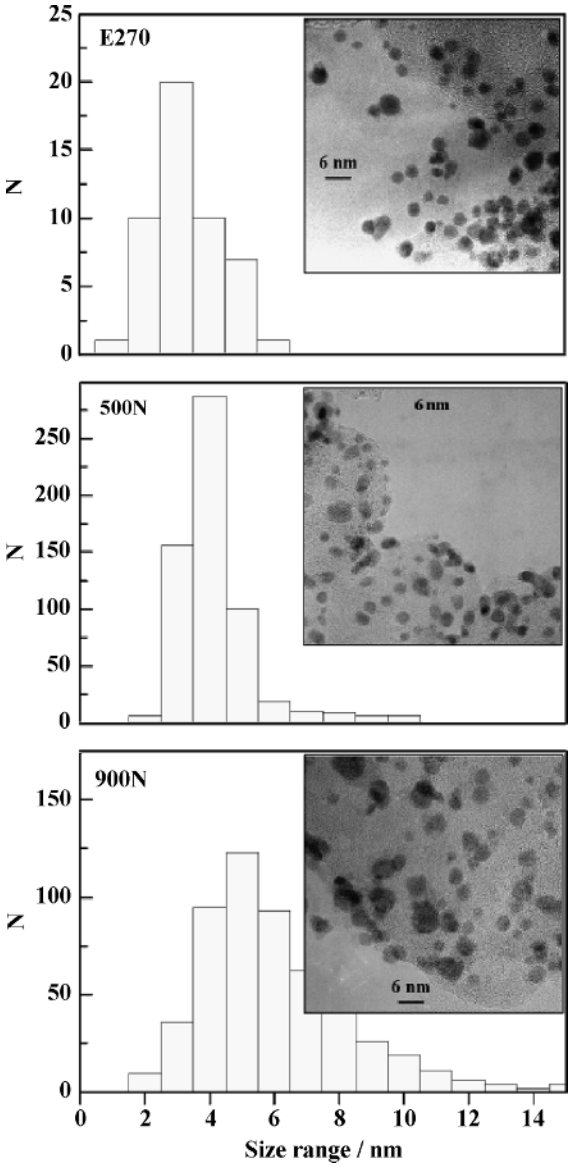

FIGURE 1.48 TEM micrographs of carbon-supported PtSn high-surface-area catalysts with corresponding histograms of particle size distribution: E270—average particle size 3–4 nm; 500N—average particle size ~4 nm; 900N—average particle size ~6 nm [197].

Polarization curves for H_2, CO, and H_2/CO oxidation are shown in Figure 1.49, where catalytic activity is expressed as mass activity (moles reactant per unit mass of Pt).

As is shown in Figure 1.49, all three catalysts show similar activities toward H_2 oxidation. However, sample E270 having a Pt : Sn atomic ratio of 3 : 1 had the highest mass activity for CO oxidation.

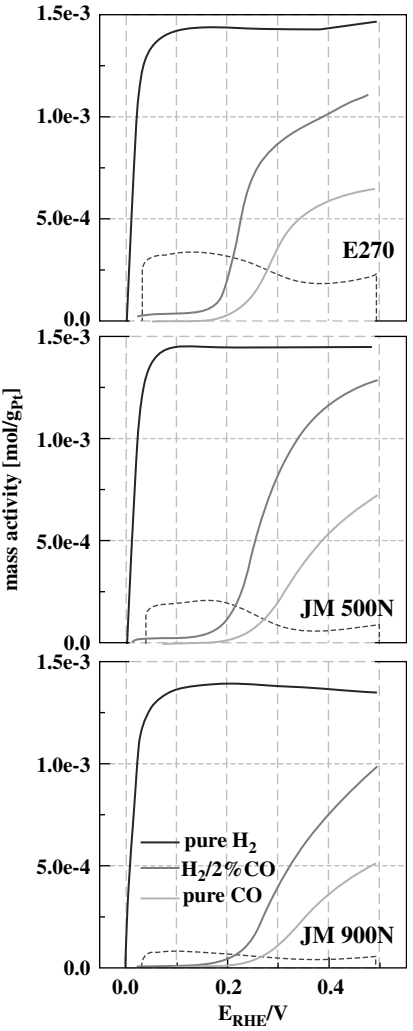

FIGURE 1.49 Polarization curves for different Pt–Sn/C catalysts recorded in 0.5 M H_2SO_4 solution saturated with either pure H_2, a H_2/2% CO mixture, or pure CO; curves are recorded at 60°C with 1 mV/s and 2500 rpm; dashed curves: CV (au) in argon-purged solution at 60°C, scan rate 50 mV/s [197].

1.7.3 HOR and HER Investigations on Highly Oriented Pyrolytic Graphite (HOPG) Systems

Highly oriented pyrolytic graphite is a carbon-based material and has been used in studying electrochemical reactions because of its interesting properties. It is a carbon material with very low surface roughness, and therefore reactions can be

studied in a model-like substrate that is closer to the "real" carbon-based catalyst systems. By investigating catalyst particles on HOPG surface, one can exclude the substrate-related effects can be due to weak binding of the metal particles to the substrate. Electrodeposited particles are not epitaxially oriented on a HOPG surface. Furthermore, because of sp^2 hybridization of carbon atoms in the HOPG basal plane, there is no possibility for bond formation between hydrogen and the surface. Therefore, hydrogen reactions on a metal-decorated HOPG surface should be affected mainly by morphological parameters, such as particle size and particle area density.

Gimeno et al. [198] utilized STM and electrochemical techniques to investigate the growth mechanism of Pd islands deposited on HOPG from aqueous solutions. They found that the initial stage of growth is under activation control followed by a diffusion

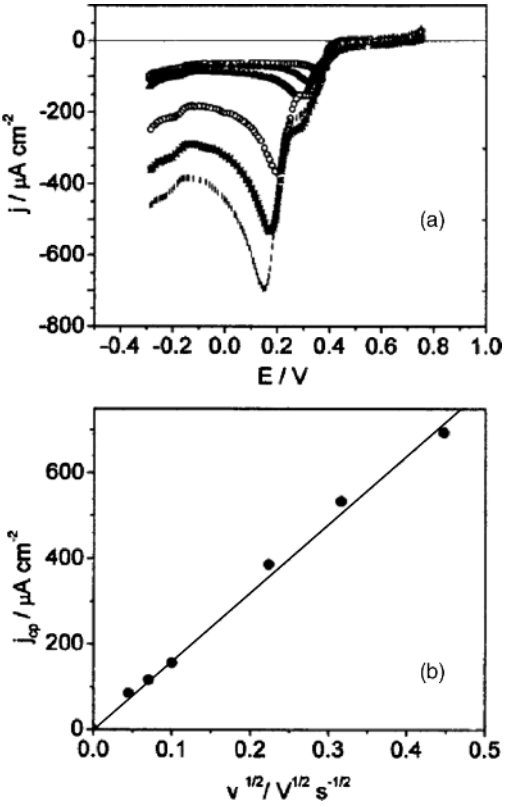

FIGURE 1.50 (a) Voltammograms obtained for HOPG in aqueous 7.5×10^{-4} $PdCl_2$ + 5 $\times 10^{-2}$M $NaClO_4$ + 5×10^{-3}M $HClO_4$ at different potential scan rates; $u = 2$ mV/s (top curve), 5 mV/s, 10 mV/s, 50 mV/s, 0.1 V/s, and 0.2 V/s (bottom curve); 298 K. (b) plot of cathodic current peak j_{cp} versus $u^{1/2}$ [198].

control. This was clearly demonstrated as shown in Figure 1.50, where the height of the cathodic current peak increases linearly with the scan rate.

Particles formed by the potential step method showed different morphologies, which strongly depended on whether the cathodic potential was above or below the potential of zero charge of the bulk palladium.

Lu and Zangari [199] studied electrodeposited Pt nanoparticles on HOPG. They investigated the different parameters during the deposition process such as the scan rate during deposition and concentration of the Pt precursor in the electrolyte. Another factor investigated was the addition of supporting electrolyte (e.g., HCl and H_2SO_4). Supporting electrolyte can influence faradaic processes and in particular, the growth and nucleation. For example, electrolytes would increase overall conductivity, resulting in compression of the double layer and shorten the double-layer charging transient. They found that chlorides in general inhibit the Pt reduction process, due to formation of adsorbed chloride films that occupy available sites for discharge of Pt complexes. On the contrary, addition of sulfate or perchlorate enhances reduction process by compressing the double layer.

Brülle and Stimming [156, 200] investigated the electrodeposition of Pt nanoparticles on HOPG surfaces and their reactivity toward HER. In order to create more active sites, an oxidation step was initially performed prior to deposition. Representative AFM images are shown in Figure 1.51.

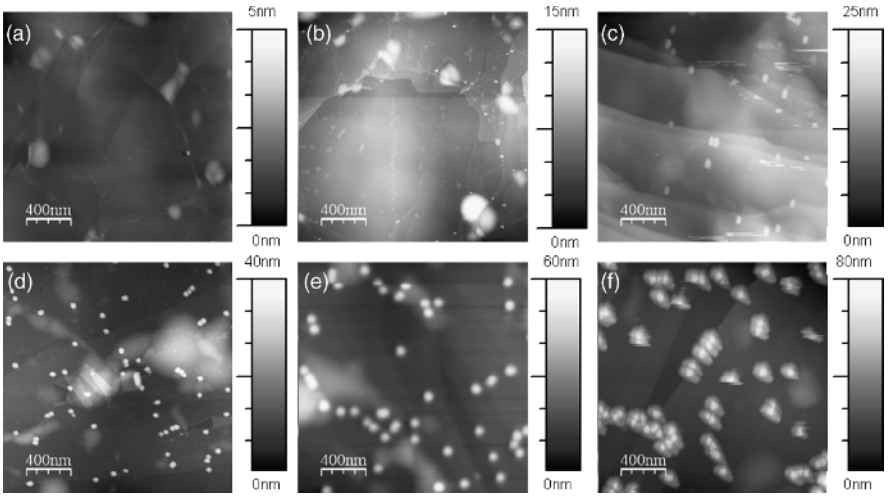

FIGURE 1.51 Tapping-mode AFM images of oxidized HOPG surfaces and Pt/HOPG samples, prepared with potentiostatic double-pulse deposition, nucleation potential $E_n = 30$ mV, nucleation time $t_n = 500$ μs, growth potential $E_g = 560$ mV, and different growth times t_g: (a) oxidized HOPG surface; (b) $t_g = 100$ s, $Q_{dep} = -2.56$ mC/cm^2; (c) $t_g = 150$ s, $Q_{dep} = -5.55$ mC/cm^2; (c) $t_g = 300$ s, $Q_{dep} = -13.76$ mC/cm^2; (d) $t_g = 450$ s, $Q_{dep} = -19.9$ mC/m^2; (e) $t_g = 600$ s, $Q_{dep} = -41.5$ mC/cm^2 [200].

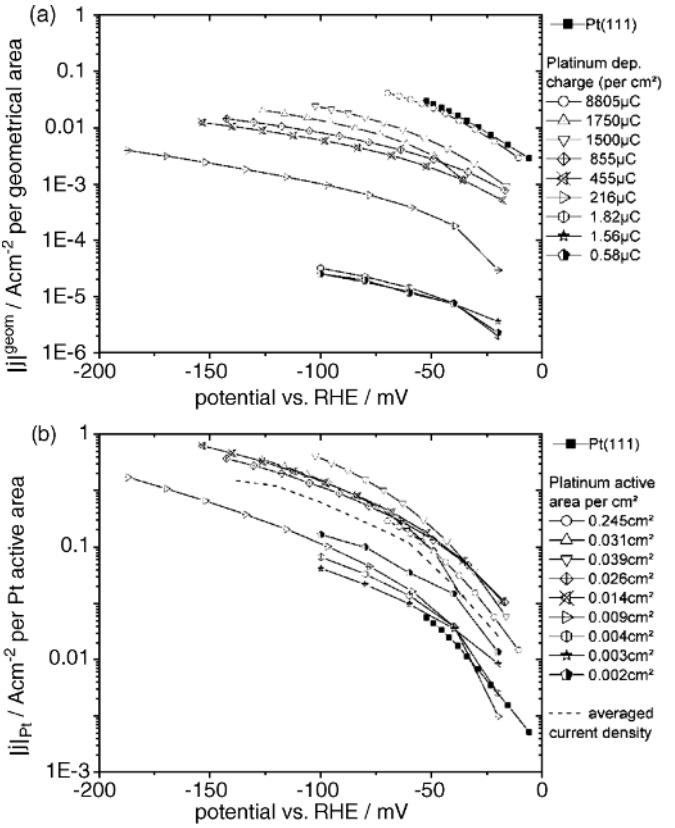

FIGURE 1.52 Tafel plots for different amounts of platinum on HOPG deposited via single-pulse method, current densities versus geometric area (a); current density normalized to platinum active area obtained from hydrogen ad/desorption charge. An averaged curve, assuming that the variation of the specific current density is due to experimental errors, is represented by the dashed line (b) [156].

HER was studied using potentiostatic pulses, and results are shown in Figure 1.52. As can be seen, the trend observed is that the more Pt is deposited, the higher the activity. For high amounts of deposited Pt, the activity reaches that from a Pt single crystal. If activities are normalized to the Pt active surface area, then they all become comparable within experimental error to Pt single crystal.

Figure 1.53 shows HER current densities normalized to platinum active surface area versus platinum coverage for Pt/Au(111) and Pt/HOPG for very small coverages (Pt surface per geometric area < 0.02). The different behavior of the activities of the two model systems becomes obvious for these small coverages. At a coverage larger than 0.01, the activity regarding HER is similar for both kinds of platinum nanostructured surfaces. For smaller amounts of platinum on Au(111) surfaces, the current densities increase sharply with decreasing coverage. For HER on Pt/HOPG, the

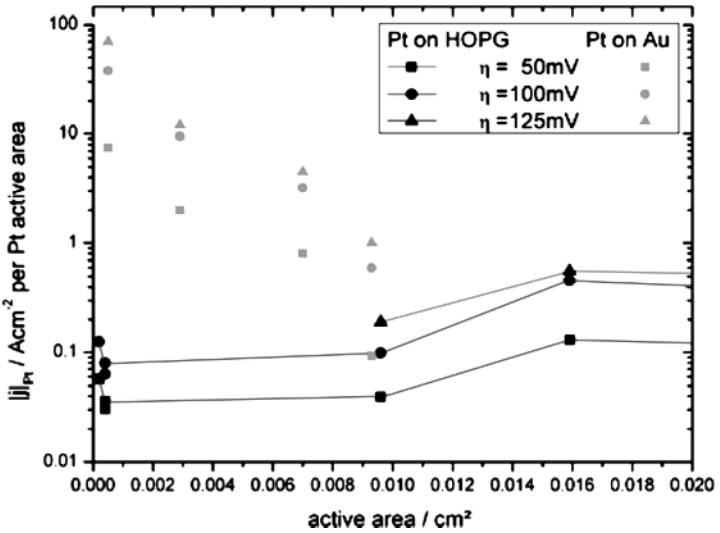

FIGURE 1.53 Current densities per platinum active area versus platinum active area per substrate (cm^{-2}) for Pt/HOPG (single-pulse method) and Pt/Au(111) for different overpotentials ($\eta = 50\,mV$, $100\,mV$, $125\,mV$) [156].

current densities do not increase but slightly decrease for decreasing coverage. This leads to the conclusion that the enhancement in reactivity for Pt/Au(111) is caused by a mechanism that cannot be applied to the Pt/HOPG model system.

REFERENCES

1. T. Erdey-Gruz and M. Volmer, *Z. Phys. Chem. Abteil. Chem. Thermodyn. Kinetik Elektrochem. Eigenschaft*. **150**, 203 (1930).
2. J. Tafel, *Z. Phys. Chem. Stochiom. Verwandt*. **50**, 641 (1905).
3. J. Heyrovsky, *Rec. Trav. Chim. Pays-Bas* **46**, 582 (1927).
4. N. M. Markovic and P. N. Ross, *Surf. Sci. Rep.* **45**, 121 (2002).
5. K. Christmann and G. Ertl, *Surf. Sci.* **60**, 365 (1976).
6. R. W. McCabe and L. D. Schmidt, *Surf. Sci.* **65**, 189 (1977).
7. M. Salmeron, R. J. Gale, and G. A. Somorjai, *J. Chem. Phys.* **70**, 2807 (1979).
8. R. A. Olsen, G. J. Kroes, and E. J. Baerends, *J. Chem. Phys.* **111**, 11155 (1999).
9. N. M. Markovic, B. N. Grgur, and P. N. Ross, *J. Phys. Chem. B* **101**, 5405 (1997).
10. J. H. Barber and B. E. Conway, *J. Electroanal. Chem.* **461**, 80 (1999).
11. J. Barber, S. Morin, and B. E. Conway, *J. Electroanal. Chem.* **446**, 125 (1998).
12. P. M. Quaino, M. R. G. de Chialvo, and A. C. Chialvo, *Phys. Chem. Chem. Phys.* **6**, 4450 (2004).
13. V. S. Bagotzky and N. V. Osetrova, *J. Electroanal. Chem.* **43**, 233 (1973).

14. P. M. Quaino, J. L. Fernandez, M. R. G. de Chialvo, and A. C. Chialvo, *J. Mol. Catal. A: Chem.* **252**, 156 (2006).
15. J. O. M. Bockris, *J. Serb. Chem. Soc.* **70**, 475 (2005).
16. B. E. Conway and J. O. Bockris, *J. Chem. Phys.* **26**, 532 (1957).
17. R. Parsons, *Trans. Faraday Soc.* **54**, 1053 (1958).
18. S. Trasatti, *J. Electroanal. Chem.* **39**, 163 (1972).
19. L. I. Krishtalik and P. Delahay eds., *Advances in Electrochemistry and Electrochemical Engineering*, Vol. 7, Interscience, New York, 1970.
20. J. K. Nørskov, T. Bligaard, A. Logadottir, J. R. Kitchin, J. G. Chen, S. Pandelov, and U. Stimming, *J. Electrochem. Soc.* **152**, J23. (2005).
21. N. M. Markovic, S. T. Sarraf, H. A. Gasteiger, and P. N. Ross, *J. Chem. Soc. Faraday Trans.* **92**, 3719 (1996).
22. N. M. Markovic, B. N. Grgur, and P. N. Ross, *J. Phys. Chem. B* **101**, 5405 (1997).
23. J. Barber, S. Morin, and B. E. Conway, *J. Electroanal. Chem.* **446**, 125 (1998).
24. J. Perez, E. R. Gonzalez, and H. M. Villullas, *J. Phys. Chem. B* **102**, 10931 (1998).
25. J. H. Barber and B. E. Conway, *J. Electroanal. Chem.* **461**, 80 (1999).
26. S. Schuldin, M. Rosen, and D. R. Flinn, *J. Electrochem. Soc.* **117**, 1251 (1970).
27. K. Seto, A. Iannelli, B. Love, and J. Lipkowski, *J. Electroanal. Chem.* **226**, 351 (1987).
28. H. Kita, S. Ye, and Y. Gao, *J. Electroanal. Chem.* **334**, 351 (1992).
29. R. Gomez, A. Fernandezvega, J. M. Feliu, and A. Aldaz, *J. Phys. Chem.* **97**, 4769 (1993).
30. J. Clavilier, R. Faure, G. Guinet, and R. Durand, *J. Electroanal. Chem.* **107**, 205 (1980).
31. J. Clavilier, *J. Electroanal. Chem.* **107**, 211 (1980).
32. S. Motoo and N. Furuya, *J. Electroanal. Chem.* **172**, 339 (1984).
33. N. Markovic, M. Hanson, G. McDougall, and E. Yeager, *J. Electroanal. Chem.* **214**, 555 (1986).
34. S. Motoo and N. Furuya, *Ber. Buns. Gesells. Phys. Chem. Chem. Phys.* **91**, 457 (1987).
35. J. Clavilier, A. Rodes, K. Elachi, and M. A. Zamakhchari, *J. Chim. Phys. Physico-Chim. Biol.* **88**, 1291 (1991).
36. J. Clavilier, J. M. Orts, and J. M. Feliu, *J. Phys. Iv* **4**, 303 (1994).
37. J. M. Feliu, A. Rodes, J. M. Orts, and J. Clavilier, *Polish J. Chem.* **68**, 1575 (1994).
38. L. A. Kibler, A. Cuesta, M. Kleinert, and D. M. Kolb, *J. Electroanal. Chem.* **484**, 73 (2000).
39. J. Clavilier, D. Armand, S. G. Sun, and M. Petit, *J. Electroanal. Chem.* **205**, 267 (1986).
40. J. Clavilier, J. M. Feliu, A. Fernandezvega, and A. Aldaz, *J. Electroanal. Chem.* **269**, 175 (1989).
41. E. Vlieg, I. K. Robinson, and K. Kern, *Surf. Sci.* **233**, 248 (1990).
42. N. M. Markovic, B. N. Grgur, C. A. Lucas, and P. N. Ross, *Surf. Sci.* **384**, L805 (1997).
43. S. Horch, H. T. Lorensen, S. Helveg, E. Laegsgaard, I. Stensgaard, K. W. Jacobsen, J. K. Nørskov, and F. Besenbacher, *Nature* **398**, 134 (1999).
44. D. A. Scherson and D. M. Kolb, *J. Electroanal. Chem.* **176**, 353 (1984).
45. A. M. Funtikov, U. Stimming, and R. Vogel, *J. Electroanal. Chem.* **428**, 147 (1997).
46. A. M. Funtikov, U. Linke, U. Stimming, and R. Vogel, *Surf. Sci.* **324**, L343 (1995).

47. L. A. Kibler, *Preparation and Characterization of Noble Metal Single Crystal Electrode Surfaces*, International Society of Electrochemistry, 2003.
48. N. M. Markovic and P. N. Ross, *Surf. Sci. Rep.* **45**, 121 (2002).
49. N. Markovic, H. Gasteiger, and P. N. Ross, *J. Electrochem. Soc.* **144**, 1591 (1997).
50. U. Frese, T. Iwasita, W. Schmickler, and U. Stimming, *J. Phys. Chem.* **89**, 1059 (1985).
51. U. Frese and U. Stimming, *J. Electroanal. Chem.* **198**, 409 (1986).
52. M. H. Dishner, M. M. Ivey, S. Gorer, J. C. Hemminger, and F. J. Feher, *J. Vac. Sci. Technol. A Vac. Surf. Films* **16**, 3295 (1998).
53. W. Haiss, D. Lackey, J. K. Sass, and K. H. Besocke, *J. Chem. Phys.* **95**, 2193 (1991).
54. D. M. Kolb, *Progress Surf. Sci.* **51**, 109 (1996).
55. O. M. Magnussen, J. Hagebock, J. Hotlos, and R. J. Behm, *Faraday Discuss.* **94**, 329 (1992).
56. G. J. Edens, X. P. Gao, and M. J. Weaver, *J. Electroanal. Chem.* **375**, 357 (1994).
57. T. Dretschkow and T. Wandlowski, *Ber. Buns. Gesell. Phys. Chem. Chem. Phys.* **101**, 749 (1997).
58. X. P. Gao, A. Hamelin, and M. J. Weaver, *Phys. Rev. B* **44**, 10983 (1991).
59. X. P. Gao, A. Hamelin, and M. J. Weaver, *Phys. Rev. Lett.* **67**, 618 (1991).
60. O. M. Magnussen, J. Hotlos, R. J. Behm, N. Batina, and D. M. Kolb, *Surf. Sci.* **296**, 310 (1993).
61. O. M. Magnussen, J. Wiechers, and R. J. Behm, *Surf. Sci.* **289**, 139 (1993).
62. A. Hamelin, *J. Electroanal. Chem.* **407**, 1 (1996).
63. M. Sturmat, R. Koch, and K. H. Rieder, *Phys. Rev. Lett.* **77**, 5071 (1996).
64. A. S. Dakkouri, *Solid State Ion.* **94**, 99 (1997).
65. G. J. Brug, M. Sluytersrehbach, J. H. Sluyters, and A. Hamelin, *J. Electroanal. Chem.* **181**, 245 (1984).
66. A. Hamelin and M. J. Weaver, *J. Electroanal. Chem.* **223**, 171 (1987).
67. A. Hamelin, L. Stoicoviciu, S. C. Chang, and M. J. Weaver, *J. Electroanal. Chem.* **307**, 183 (1991).
68. S. Trasatti, *Russ. J. Electrochem.* **41**, 1255 (2005).
69. M. Baldauf and D. M. Kolb, *Electrochim. Acta* **38**, 2145 (1993).
70. L. A. Kibler, M. Kleinert, R. Randler, and D. M. Kolb, *Surf. Sci.* **443**, 19 (1999).
71. L. A. Kibler, M. Kleinert, and D. M. Kolb, *Surf. Sci.* **461**, 155 (2000).
72. H. Naohara, S. Ye, and K. Uosaki, *Electrochim. Acta* **45**, 3305 (2000).
73. B. Alvarez, V. Climent, A. Rodes, and J. M. Feliu, *Phys. Chem. Chem. Phys.* **3**, 3269 (2001).
74. H. Naohara, S. Ye, and K. Uosaki, *J. Electroanal. Chem.* **500**, 435 (2001).
75. L. A. Kibler, M. Kleinert, V. Lazarescu, and D. M. Kolb, *Surf. Sci.* **498**, 175 (2002).
76. R. Hoyer, L. A. Kibler, and D. M. Kolb, *Electrochim. Acta* **49**, 63 (2003).
77. L. A. Kibler, A. M. El-Aziz, and D. M. Kolb, *J. Mol. Catal. A Chem.* **199**, 57 (2003).
78. M. Arenz, V. Stamenkovic, P. N. Ross, and N. M. Markovic, *Surf. Sci.* **573**, 57 (2004).
79. A. M. El-Aziz, R. Hoyer, L. A. Kibler, and D. M. Kolb, *Electrochim. Acta* **51**, 2518 (2006).
80. S. Pandelov and U. Stimming, *Electrochim. Acta* **52**, 5548 (2007).
81. Y. Pluntke, L. A. Kibler, and D. M. Kolb, *Phys. Chem. Chem. Phys.* **10**, 3684 (2008).

82. H. Wolfschmidt, R. Bussar, and U. Stimming, *J. Phys. Condens. Matt.* **20**, 374127 (2008).
83. B. Hammer and J. K. Nørskov, *Surf. Sci.* **343**, 211 (1995).
84. B. Hammer, Y. Morikawa, and J. K. Nørskov, *Phys. Rev. Lett.* **76**, 2141 (1996).
85. M. Mavrikakis, B. Hammer, and J. K. Nørskov, *Phys. Rev. Lett.* **81**, 2819 (1998).
86. B. Hammer and J. K. Nørskov, in *Chemisorption and Reactivity on Supported Cluster and Thin Films*, R. M. Lambert, G. Pacchiani, eds., Kluwer, Netherlands, 1997.
87. J. K. Nørskov, T. Bligaard, A. Logadottir, J. R. Kitchin, J. G. Chen, S. Pandelov, and U. Stimming, *J. Electrochem. Soc.* **152**, J23 (2005).
88. V. Pallassana, M. Neurock, L. B. Hansen, B. Hammer, and J. K. Nørskov, *Phys. Rev. B* **60**, 6146 (1999).
89. V. Pallassana, M. Neurock, L. B. Hansen, and J. K. Nørskov, *J. Chem. Phys.* **112**, 5435 (2000).
90. B. Hammer and J. K. Nørskov, *Adv. Catal.* **45**, 71 (2000).
91. A. Roudgar and A. Gross, *Phys. Rev. B* **67**, 033409 (2003).
92. A. Roudgar and A. Gross, *J. Electroanal. Chem.* **548**, 121 (2003).
93. M. Eikerling, J. Meier, and U. Stimming, *Z. Phys. Chem.* **217**, 395 (2003).
94. J. Greeley, T. F. Jaramillo, J. Bonde, I. B. Chorkendorff, and J. K. Nørskov, *Nature Mater* **5**, 909 (2006).
95. J. Greeley, J. K. Nørskov, L. A. Kibler, A. M. El-Aziz, and D. M. Kolb, *ChemPhysChem* **7**, 1032 (2006).
96. J. Greeley and J. K. Nørskov, *Surf. Sci.* **601**, 1590 (2007).
97. E. Santos, K. Potting, and W. Schmickler, *Faraday Discuss* **140**, 209 (2008).
98. E. Santos and W. Schmickler, *Angew. Chem. Int. Ed.* **46**, 8262 (2007).
99. E. Santos and W. Schmickler, *Chem. Phys.* **332**, 39 (2007).
100. E. Santos and W. Schmickler, *Electroch. Acta* **53**, 6149 (2008).
101. J. M. Ogden, M. M. Steinbugler, and T. G. Kreutz, *J. Power Sources* **79**, 143 (1999).
102. L. Carrette, K. A. Friedrich, and U. Stimming, *ChemPhysChem* **1**, 162 (2000).
103. N. M. Markovic and P. N. Ross, *Surf. Sci. Rep.* **45**, 121 (2002).
104. M. Z. Jacobson, W. G. Colella, and D. M. Golden, *Science* **308**, 1901 (2005).
105. J. O. M. Bockris, *J. Serb. Chem. Soc.* **70**, 475 (2005).
106. B. E. Conway and J. O. Bockris, *J. Chem. Phys.* **26**, 532 (1957).
107. R. Parsons, *Trans. Faraday Soc.* **54**, 1053 (1958).
108. H. Gerischer, *Angew. Chem. Int. Ed.* **70**, 107 (1958).
109. S. Trasatti, *J. Electroanal. Chem.* **39**, 163 (1972).
110. P. Sabatier, *Ber. Dtsch. Chem. Gesells.* **44**, 1984 (1911).
111. B. Hammer and J. K. Nørskov, *Surf. Sci.* **343**, 211 (1995).
112. A. Ruban, B. Hammer, P. Stoltze, H. L. Skriver, and J. K. Nørskov, *J. Mol. Catal. A Chem.* **115**, 421 (1997).
113. A. Roudgar and A. Gross, *Surf. Sci.* **597**, 42 (2005).
114. D. Menzel, *Science* **295**, 58 (2002).
115. P. J. Feibelman, *Science* **295**, 99 (2002).
116. P. J. Feibelman, *Phys. Rev. Lett.* **90**, 2003.

117. B. E. Conway, E. M. Beatty, and P. A. D. DeMaine, *Electrochim. Acta* **7**, 39 (1962).
118. J. Meier, K. A. Friedrich, and U. Stimming, *Faraday Discuss.* **121**, 365 (2002).
119. L. A. Kibler, M. Kleinert, R. Randler, and D. M. Kolb, *Surf. Sci.* **443**, 19 (1999).
120. M. Baldauf and D. M. Kolb, *J. Phys. Chem.* **100**, 11375 (1996).
121. M. Baldauf and D. M. Kolb, *Electrochim. Acta* **38**, 2145 (1993).
122. R. Hoyer, L. A. Kibler, and D. M. Kolb, *Electrochim. Acta* **49**, 63 (2003).
123. H. Naohara, S. Ye, and K. Uosaki, *J. Phys. Chem. B* **102**, 4366 (1998).
124. R. Hoyer, L. A. Kibler, and D. M. Kolb, *Surf. Sci.* **562**, 275 (2004).
125. S. R. Brankovic, J. McBreen, and R. R. Adzic, *Surf. Sci.* **479**, L363 (2001).
126. J. Tang, M. Petri, L. A. Kibler, and D. M. Kolb, *Electrochim. Acta* **51**, 125 (2005).
127. L. A. Kibler, A. M. El-Aziz, R. Hoyer, and D. M. Kolb, *Angew. Chem. Int. Ed.* **44**, 2080 (2005).
128. L. A. Kibler, A. M. El-Aziz, and D. M. Kolb, *J. Mol. Catal. A Chem.* **199**, 57 (2003).
129. B. Hammer and J. K. Nørskov, *Surf. Sci.* **343**, 211 (1995).
130. A. Ruban, B. Hammer, P. Stoltze, H. L. Skriver, and J. K. Nørskov, *J. Mol. Catal. A Chem.* **115**, 421 (1997).
131. J. Meier, PhD thesis, Technische Univ. München, 2003.
132. J. Meier, K. A. Friedrich, and U. Stimming, *Faraday Discuss.* **121**, 365 (2002).
133. J. Meier, J. Schiotz, P. Liu, J. K. Nørskov, and U. Stimming, *Chem. Phys. Lett.* **390**, 440 (2004).
134. S. Pandelov and U. Stimming, *Electrochim. Acta* **52**, 5548 (2007).
135. L. A. Kibler, *ChemPhysChem* **7**, 985 (2006).
136. J. Greeley, T. F. Jaramillo, J. Bonde, I. B. Chorkendorff, and J. K. Nørskov, *Nature Mater.* **5**, 909 (2006).
137. B. Hammer and J. K. Nørskov, *Adv. Catal.* **45**, 71 (2000).
138. B. Hammer and J. K. Nørskov, *Surf. Sci.* **343**, 211 (1995).
139. J. K. Nørskov, *Reac. Kinet. Dev. Catal. Process.* **122**, 3 (1999).
140. J. K. Nørskov, T. Bligaard, A. Logadottir, J. R. Kitchin, J. G. Chen, S. Pandelov, and U. Stimming, *J. Electrochem. Soc.* **152**, J23 (2005).
141. H. Wolfschmidt, R. Bussar, and U. Stimming, *J. Phys. Condens. Matt.* **20**, 374127 (2008).
142. N. M. Markovic and P. N. Ross, *Surf. Sci. Rep.* **45**, 121 (2002).
143. N. M. Markovic, C. A. Lucas, V. Climent, V. Stamenkovic, and P. N. Ross, *Surf. Sci.* **465**, 103 (2000).
144. F. Hernandez and H. Baltruschat, *J. Solid State Electrochem.* **11**, 877 (2007).
145. F. Hernandez and H. Baltruschat, *Langmuir* **22**, 4877 (2006).
146. J. Steidtner, F. Hernandez, and H. Baltruschat, *J. Phys. Chem. C* **111**, 12320 (2007).
147. M. Eikerling, J. Meier, and U. Stimming, *Z. Phys. Chem.* **217**, 395 (2003).
148. M. Mavrikakis, B. Hammer, and J. K. Nørskov, *Phys. Rev. Lett.* **81**, 2819 (1998).
149. A. Roudgar and A. Gross, *Phys. Rev. B* **67**, 033409 (2003).
150. A. Roudgar and A. Gross, *J. Electroanal. Chem.* **548**, 121 (2003).
151. J. Greeley, J. K. Nørskov, and M. Mavrikakis, *Annu. Rev. Phys. Chem.* **53**, 319 (2002).
152. J. R. Kitchin, J. K. Nørskov, M. A. Barteau, and J. G. Chen, *Phys. Rev. Lett.* **93**, 156801 (2004).

153. A. Roudgar and A. Gross, *J. Electroanal. Chem.* **548**, 121 (2003).
154. A. V. Ruban, H. L. Skriver, and J. K. Nørskov, *Phys. Rev. B* **59**, 15990 (1999).
155. C. Camus, diploma thesis, Technische Univ. München (Garching), 2004.
156. T. Brülle and U. Stimming, *J. Electroanal. Chem.* **636**, 10 (2009).
157. L. A. Kibler, *ChemPhysChem* **7**, 985 (2006).
158. L. A. Kibler, A. M. El-Aziz, and D. M. Kolb, *J. Mol. Catal. A Chem.* **199**, 57 (2003).
159. N. M. Markovic, C. A. Lucas, V. Climent, V. Stamenkovic, and P. N. Ross, *Surf. Sci.* **465**, 103 (2000).
160. N. M. Markovic and P. N. Ross, *Surf. Sci. Rep.* **45**, 121 (2002).
161. S. Pandelov and U. Stimming, *Electrochim. Acta* **52**, 5548 (2007).
162. H. Wolfschmidt, R. Bussar, and U. Stimming, *J. Phys. Condens. Matt.* **20**, 374127 (2008).
163. M. Baldauf and D. M. Kolb, *Electrochim. Acta* **38**, 2145 (1993).
164. J. Meier, K. A. Friedrich, and U. Stimming, *Faraday Discuss*. **121**, 365 (2002).
165. J. Meier, J. Schiotz, P. Liu, J. K. Norskov, and U. Stimming, *Chem. Phys. Lett.* **390**, 440 (2004).
166. M. Petri and D. M. Kolb, *Phys. Chem. Chem. Phys.* **4**, 1211 (2002).
167. Z. X. Xie and D. M. Kolb, *J. Electroanal. Chem.* **481**, 177 (2000).
168. S. G. Garcia, D. R. Salinas, C. E. Mayer, W. J. Lorenz, and G. Staikov, *Electrochim. Acta* **48**, 1279 (2003).
169. R. Schuster, V. Kirchner, P. Allongue, and G. Ertl, *Science* **289**, 98 (2000).
170. V. Kirchner, L. Cagnon, R. Schuster, and G. Ertl, *Appl. Phys. Lett.* **79**, 1721 (2001).
171. W. Schindler, D. Hofmann, and J. Kirschner, *J. Appl. Phys.* **87**, 7007 (2000).
172. R. T. Potzschke, G. Staikov, W. J. Lorenz, and W. Wiesbeck, *J. Electrochem. Soc.* **146**, 141 (1999).
173. W. Schindler, D. Hofmann, and J. Kirschner, *J. Electrochem. Soc.* **148**, C124(2001).
174. A. J. Bard and M. V. Mirkin, *Scanning Electrochemical Microscopy*, Wiley, New York, 2001.
175. N. Baltes, L. Thouin, C. Amatore, and J. Heinze, *Angew. Chem. Int. Ed.* **43**, 1431 (2004).
176. G. E. Engelmann, J. C. Ziegler, and D. M. Kolb, *Surf. Sci*. **401**, L420(1998).
177. M. G. Del Popolo, E. P. M. Leiva, H. Kleine, J. Meier, U. Stimming, M. Mariscal, and W. Schmickler, *Electrochim. Acta* **48**, 1287 (2003).
178. D. M. Kolb, R. Ullmann, and T. Will, *Science* **275**, 1097 (1997).
179. D. M. Kolb, R. Ullmann, and J. C. Ziegler, *Electrochim. Acta* **43**, 2751 (1998).
180. M. Del Popolo, E. Leiva, H. Kleine, J. Meier, U. Stimming, M. Mariscal, and W. Schmickler, *Appl. Phys. Lett.* **81**, 2635 (2002).
181. D. M. Kolb and F. C. Simeone, *Electrochim. Acta* **50**, 2989 (2005).
182. D. M. Kolb, G. E. Engelmann, and J. C. Ziegler, *Angew. Chem. Int. Ed.* **39**, 1123 (2000).
183. G. E. Engelman, J. C. Ziegler, and D. M. Kolb, *J. Electrochem. Soc.* **145**, 2970 (1998).
184. D. M. Kolb, G. E. Engelmann, and J. C. Ziegler, *Solid State Ion*. **131**, 69 (2000).
185. D. M. Kolb, J. C. Ziegler, and G. E. Engelmann, *Abstr. Papers Am. Chem. Soc* **219**, U347 (2000).
186. R. Ullmann, T. Will, and D. M. Kolb, *Chem. Phys. Lett.* **209**, 238 (1993).

187. R. Ullmann, T. Will, and D. M. Kolb, *Ber. Buns. Gesell. Phys. Chem. Chem. Phys.* **99**, 1414 (1995).
188. W. Schindler, P. Hugelmann, A. Hugelmann, and F. Kartner, *J. Electroanal. Chem.* **522**, 49 (2002).
189. M. Eikerling, J. Meier, and U. Stimming, *Z. Phys. Chem.* **217**, 395 (2003).
190. B. Hammer and J. K. Nørskov, *Adv. Catal.* **45**, 71 (2000).
191. A. Ruban, B. Hammer, P. Stoltze, H. L. Skriver, and J. K. Nørskov, *J. Mol. Catal. A Chem.* **115**, 421 (1997).
192. O. Savadogo, K. Amuzgar, and D. L. Piron, *Int. J. Hydrogen Energy* **15**, 783 (1990).
193. H. Naohara, S. Ye, and K. Uosaki, *J. Phys. Chem. B* **102**, 4366 (1998).
194. H. A. Gasteiger, N. M. Markovic, and P. N. Ross, *J. Phys. Chem.* **99**, 16757 (1995).
195. K. Sasaki, Y. Mo, J. X. Wang, M. Balasubramanian, F. Uribe, J. McBreen, and R. R. Adzic, *Electrochim. Acta* **48**, 3841 (2003).
196. S. L. Chen and A. Kucernak, *J. Phys. Chem. B* **108**, 13984 (2004).
197. M. Arenz, V. Stamenkovic, B. B. Blizanac, K. J. Mayrhofer, N. M. Markovic, and P. N. Ross, *J. Catal.* **232**, 402 (2005).
198. Y. Gimeno, A. H. Creus, P. Carro, S. Gonzalez, R. C. Salvarezza, and A. J. Arvia, *J. Phys. Chem. B* **106**, 4232 (2002).
199. G. J. Lu and G. Zangari, *J. Phys. Chem. B* **109**, 7998 (2005).
200. T. Brülle and U. Stimming, in preparation.